

Article

First Principles Thermodynamics of Minerals at HP–HT Conditions: MgO as a Prototypical Material

Donato Belmonte

Dipartimento di Scienze della Terra, dell’Ambiente e della Vita (DISTAV), University of Genova, Corso Europa 26, 16132 Genova, Italy; donato.belmonte@unige.it; Tel.: +39-010-3538136

Received: 21 August 2017; Accepted: 25 September 2017; Published: 28 September 2017

Abstract: Ab initio thermodynamic properties, equation of state and phase stability of periclase (MgO, B1-type structure) have been investigated in a broad P–T range (0–160 GPa; 0–3000 K) in order to set a model reference system for phase equilibria simulations under deep Earth conditions. Phonon dispersion calculations performed on large supercells using the finite displacement method and in the framework of quasi-harmonic approximation highlight the performance of the Becke three-parameter Lee–Yang–Parr (B3LYP) hybrid density functional in predicting accurate thermodynamic functions (heat capacity, entropy, thermal expansivity, isothermal bulk modulus) and phase reaction boundaries at high pressure and temperature. A first principles Mie–Grüneisen equation of state based on lattice vibrations directly provides a physically-consistent description of thermal pressure and P–V–T relations without any need to rely on empirical parameters or other phenomenological formalisms that could give spurious anomalies or uncontrolled extrapolations at HP–HT. The post-spinel phase transformation, Mg_2SiO_4 (ringwoodite) = MgO (periclase) + MgSiO₃ (bridgmanite), is taken as a computational example to illustrate how first principles theory combined with the use of hybrid functionals is able to provide sound results on the Clapeyron slope, density change and P–T location of equilibrium mineral reactions relevant to mantle dynamics.

Keywords: ab initio; thermodynamics; MgO; phase equilibrium; equation of state; high pressure; high temperature; hybrid DFT; post-spinel transformation

1. Introduction

Building a reliable mineralogical model for the deep Earth and planetary interiors requires accurate knowledge of thermodynamic properties of the constituent phases at extreme conditions of pressure and temperature in order to obtain meaningful stability relations. Most of the attempts made so far in the literature [1–8] rely on phase equilibrium models, which are based on the assessment of experimental datasets, while very few of them use first principles data to calculate phase diagrams [9–12]. However, a full ab initio thermodynamic database for phase equilibria calculation at high pressure and temperature (HP–HT) has not been created yet, even for simple compositional systems. The first step to achieving this goal is predicting the thermodynamic properties of the main mineralogical constituents, and using them to define P–T stability fields and model phase transition and reaction boundaries by Gibbs free energy minimization. This, in turn, provides the energetic ground to understand the role of phase stability on the origin of seismic discontinuities and large-scale geodynamic processes in the deep Earth [13,14].

Periclase (MgO with *fcc* or B1-type cubic structure), along with with silicate perovskites (bridgmanite and Ca-perovskite), is one of the main constituents of the Earth’s lower mantle [15] and, much more than silicate perovskites, controls its rheological properties [16]. Due to its simple structure and large stability field, it has always been considered to be a milestone for computational investigation, also because of the possibility of comparing calculations with a great variety of experimental data in

a broad range of P–T conditions. Nevertheless, despite this apparent simplicity, MgO could display complex features under HP–HT conditions (like a strong single-crystal elastic anisotropy [17,18]), and some aspects related to its thermodynamic and thermophysical properties under those conditions are still poorly defined [19].

In this work a first principles, comprehensive thermodynamic investigation of MgO is carried out up to HP–HT conditions (i.e., 0–160 GPa; 0–3000 K) using hybrid density functional theory (DFT). Hybrid functionals, such as B3LYP [20], have been shown to provide excellent results, and a real improvement with respect to pure local density approximation (LDA) and generalized-gradient approximation (GGA) methods with regard to the simulation of elastic, vibrational and thermodynamic properties of insulating solids (such as Mg–Al silicates and oxides) at HP–HT conditions [21–25]. A comparison between ab initio thermodynamic properties of minerals calculated by hybrid functionals and state-of-the-art experimental results obtained by calorimetry, vibrational spectroscopy and X-ray diffraction techniques has been made by several studies in the literature, which have pointed out that the level of accuracy is within 1–2%, on average, for the majority of thermodynamic properties [26–33]. On the other hand, the main sources of error (such as volume overestimate in GGA-based DFT calculations), are usually well-known and under control [34–36].

Some key aspects on the thermodynamics of MgO are emphasized in this work. First, a detailed survey on the accuracy of quasi-harmonic lattice dynamics calculations performed on large supercells with the B3LYP hybrid density functional is carried out by comparing the results obtained on thermodynamic and thermophysical properties (i.e., heat capacities, entropy, bulk moduli, thermal expansivity, Grüneisen parameter) with selected experimental data and other theoretical calculations. Second, a first principles Mie–Grüneisen equation of state (FPMG-EOS) based on lattice dynamics is developed to provide physically-consistent P–V–T relations for solids at HP–HT conditions and the results are compared with those obtained by the use of a finite strain equation of state (like the 3rd order Birch–Murnaghan EOS). Finally, the computed thermodynamic dataset is used to predict the phase equilibrium boundary of the post-spinel transformation, Mg_2SiO_4 (ringwoodite) = MgO (periclase) + MgSiO₃ (bridgmanite), which is one of the most relevant to the physics of the Earth's interior.

2. Materials and Methods

Ab initio calculations in this work have been performed with the CRYSTAL14 code [37] by using an all-electron Gaussian-type basis set and the hybrid B3LYP functional [19,38]. Hybrid functionals, which contain a fraction of exact Hartree–Fock exchange (i.e., 20% in the case of B3LYP) mixed to the GGA exchange–correlation, are widely and successfully used in solid-state chemistry [34,35].

Magnesium and oxygen are described by (8s)-(511sp)-(1d) and (8s)-(411sp)-(1d) contractions, respectively. The exponents (in bohr⁻²) of the most diffuse functions are $\alpha_{\text{sp}} = 0.2245$ and $\alpha_{\text{d}} = 0.50$ for Mg, $\alpha_{\text{sp}} = 0.181$ and $\alpha_{\text{d}} = 0.60$ for O. These basis functions have been optimized and successfully used in previous works on magnesium silicates [23,28,31,33].

The level of accuracy in evaluating the Coulomb and Hartree–Fock exchange series is controlled by five parameters [37], for which the 8 8 8 9 18 values are used here. The threshold on the self-consistent field (SCF) energy is set to 10⁻⁸ Hartree for geometry optimization and equation of state calculation, and to 10⁻¹⁰ Hartree for computation of vibrational frequencies. The reciprocal space is sampled according to a regular sublattice of k-points according to the Monkhorst–Pack scheme [39]. The sampling of electronic states in the reciprocal space is defined by a shrinking factor set to 8 (along the three lattice vectors) [37], corresponding to 29 independent k vectors in the irreducible part of the Brillouin zone (BZ). The DFT exchange–correlation contribution is evaluated by numerical integration over the unit cell volume. In CRYSTAL, radial and angular points of the grid are generated through Gauss–Legendre radial quadrature and Lebedev two-dimensional angular point distributions. A (75,974)p grid is used, corresponding to a pruned grid with 75 radial and 974 angular points (see [37] for details). Accuracy in the integration can be estimated by the error $\Delta\epsilon$

on the integrated electronic charge density in the unit cell (i.e., $\Delta e = 4 \times 10^{-5}$ on a total of 20 electrons per unit cell).

Geometry optimization is performed by using analytical energy gradients with respect to atomic coordinates and unit cell parameters within a quasi-Newton scheme combined with the Broyden-Fletcher-Goldfarb-Shanno (BFGS) algorithm for Hessian updating [40–42]. Convergence is tested on the root-mean-square (RMS) and the absolute value of the largest component of both the gradients and nuclear displacements. The thresholds for RMS forces and nuclear displacements are set to 0.00015 a.u. and 0.0001 a.u., which are 2 and 10 times more severe than the default values, respectively [37].

The calculation of the vibrational frequencies at the Γ point of the BZ (i.e., $\mathbf{k} = \mathbf{0}$) is performed within the harmonic approximation by constructing the mass-weighted Hessian matrix via numerical integration of the analytical gradients with respect to the atomic Cartesian coordinates (see [43] for further details). The optimized equilibrium geometry is taken as reference for the calculation of vibrational frequencies. Phonon dispersion calculations at \mathbf{k} -points other than Γ are performed on large supercells with a direct-space approach [44,45], as implemented in the CRYSTAL14 program [37]. The \mathbf{k} -point mesh used to sample the reciprocal space in phonon dispersion calculation is different from that used for the electronic states, as it depends from the shape and the size of the adopted supercell. In general, the bigger the supercell, the denser the sampling of the phonon dispersion in reciprocal space. To check the numerical convergence of thermodynamic properties, isotropic supercells of increasing size have been considered (see below): a $5 \times 5 \times 5$ supercell with 250 atoms and 750 normal modes sampled at 125 \mathbf{k} -points in the first BZ turns out to be enough to ensure convergence on harmonic thermodynamic functions (e.g., isochoric heat capacity and vibrational entropy) in the whole P–T range.

Mode-gamma Grüneisen parameters (γ_i), which define the volume dependence of the vibrational frequencies in the framework of the quasi-harmonic approximation (QHA), are computed by least-square fitting of the vibrational frequencies determined at eight different volume conditions (i.e., $V/V_0 = 0.65, 0.70, 0.75, 0.80, 0.85, 0.90, 0.95$ and 1.00). Third-order polynomial fitting turns out to accurately describe the volume dependence of all the vibrational frequencies at different \mathbf{k} -points in the first BZ. The same volume conditions are then considered to calculate zero-point correction and thermal pressure contributions and define the full set of P–V–T relations of MgO.

3. Results and Discussion

Selected results obtained for thermophysical and thermodynamic properties and P–V–T equation of state of periclase in a broad range of P–T conditions (i.e., 0–160 GPa; 0–3000 K) are presented and discussed in the following sections. The computed dataset is then used to simulate the post-spinel reaction boundary, Mg_2SiO_4 (ringwoodite) = MgO (periclase) + MgSiO_3 (bridgmanite), and hence to test the capability of ab initio thermodynamic data to predict reliable phase equilibria under deep Earth conditions.

3.1. Thermal Expansion and Thermophysical Properties

Thermophysical properties of solids can be derived by the statistical mechanics analysis of vibrational modes of the crystal lattice [46]. The Helmholtz free energy, $F(V, T)$, for instance, can be expressed as:

$$F(V, T) = U_0(V) + \frac{1}{2} \sum_{i=1}^{3n} h\nu_i + kT \sum_{i=1}^{3n} \ln \left(1 - e^{-\frac{h\nu_i}{kT}} \right) \quad (1)$$

where $U_0(V)$ is the static energy calculated at different volumes (the so-called “potential well”); h and k are the Planck and Boltzmann constants, respectively; n represents the number of atoms in

the (primitive) unit cell of the crystal; ν_i is the frequency of the i^{th} vibrational mode in the crystal lattice; and

$$U_{\text{ZPC}}(V) = \frac{1}{2} \sum_{i=1}^{3n} h\nu_i \quad (2)$$

is the zero-point correction energy related to the atomic vibrations at $T = 0$ K. By applying the thermodynamic identity:

$$\alpha K_T = \left(\frac{\partial P}{\partial T} \right)_V = - \frac{\partial}{\partial V} \left[\left(\frac{\partial F}{\partial T} \right)_V \right]_T \quad (3)$$

we obtain the following expression of the product αK_T (i.e., the coefficient of volume thermal expansion or thermal expansivity, α , times the isothermal bulk modulus, K_T):

$$\alpha K_T(V, T) = \frac{R}{ZV} \sum_{i=1}^{3n} \gamma_i e^{X_i} \left(\frac{X_i}{e^{X_i} - 1} \right)^2 \quad (4)$$

where $R = kN_0$ is the universal gas constant (N_0 is the Avogadro number); Z is the number of unit formula in the (primitive) unit cell; V is the molar volume (in J/bar); X_i is the adimensionalized frequency, defined as:

$$X_i = \frac{h\nu_i}{kT} \quad (5)$$

and γ_i is the mode-gamma Grüneisen parameter of the i^{th} vibrational mode of the crystal lattice, defining its volume dependence in the framework of quasi-harmonic approximation (QHA) [47], i.e.,

$$\gamma_i = - \frac{\partial \ln \nu_i}{\partial \ln V} \quad (6)$$

If the summation in Equation (4) is taken over all the vibrational modes sampled at discrete \mathbf{k} -points in the first BZ, Equation (4) can be rewritten as:

$$\alpha K_T(V, T) = \frac{R}{ZV} \sum_{\vec{k}, i=1}^{3n} \gamma_i(\vec{k}, V) e^{X_i(\vec{k}, V)} \left(\frac{X_i(\vec{k}, V)}{e^{X_i(\vec{k}, V)} - 1} \right)^2 \quad (7)$$

Both the effect of phonon dispersion and the contribution of the acoustic modes are thus straightforwardly included in Equation (7).

The values calculated for the product αK_T of MgO are shown in Figure 1. The ab initio quasi-harmonic calculation reproduces well the experimental data [48,49] and thermodynamic assessments [50,51] up to the Debye temperature of the phase (i.e., $\Theta_D = 945$ K); then, a deviation occurs due to a common drawback of QHA at low-pressure and high-temperature conditions. In particular, while experimental observations point out a decrease of αK_T values beyond $T \approx 1000$ K, ab initio results attain an asymptotic value due to the functional form of Equation (4) or (7).

Once the values of the product αK_T are known, thermal expansivity (α) can be calculated from the values of K_T (i.e., the isothermal bulk modulus at discrete T conditions). The latter can be obtained by fitting F - V - T (or P - V - T) values according to:

$$K_T = -V \left(\frac{\partial P}{\partial V} \right)_T = V \left(\frac{\partial^2 F}{\partial V^2} \right)_T \quad (8)$$

So, once free energies at different volumes are available (cf. Equation (1)), one can proceed with the finite difference calculation of the second derivatives of the free energy to derive K_T . In principle, this should be the best choice, but a practical problem is that the amount of F - V - T data to fit is usually not so high, due to the high computational cost of full phonon dispersion calculations.

Another problem is that the definition of K'_T (i.e., the T-dependence of the bulk modulus pressure derivative or, in other words, the mixed P–T derivative of the bulk modulus) is often poor, and is affected by large uncertainties [52], so that K' is often assumed to be independent of temperature (which is not always the case). There are two different ways to overcome these problems. The first is to use the polynomial functions which define the mode-gamma Grüneisen parameters in Equation (6) to fit the vibrational frequencies under any volume conditions, and then to detail the grid of F–V–T (or P–V–T) data. The second is to use a phenomenological EOS formalism (like the 3rd- or 4th-order Birch-Murnaghan equation of state, BM3-EOS or BM4-EOS) to fit the data and derive the thermoelastic parameters [53,54]; this is a common practice in both experimental and computational works [55,56] and, in principle, allows for the determination of K'_T values, too. The basic difference between the two approaches is that the former is mostly numerical, while the latter is fully analytical.

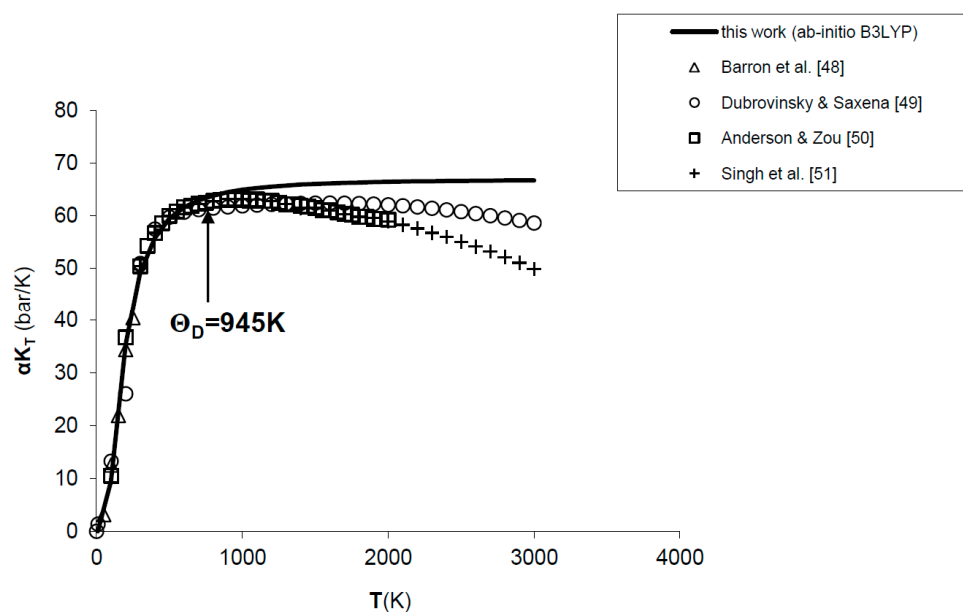


Figure 1. Ab initio B3LYP results for the product αK_T of MgO, as compared to experimental data [48,49] and thermodynamic assessments [50,51]. $\Theta_D = 945$ K is the Debye temperature.

The ab initio results of K_T and K'_T obtained for MgO in this work, as compared to experimental measurements and other theoretical calculations, are shown in Tables 1 and 2 and Figure 2.

Ab initio B3LYP values of K_T , as obtained by a full phonon dispersion calculation of P–V–T relations fitted with a BM3-EOS (see Section 3.3), are in excellent agreement with the experimental results determined by rectangular parallelepiped resonance technique in the range $T = 300$ – 1800 K at $P = 1$ bar [57] (see Figure 2). Although theoretical data taken from the literature are quite scattered, B3LYP results compare favorably both with LDA results [58,59] and semi-empirical molecular dynamics [60], while GGA values seem to be overestimated over the whole T range [61] (see Table 1 and Figure 2). As expected, K_T values slightly deviate from MD results beyond $T \approx 2000$ K, which roughly corresponds to 2/3 of the melting temperature of MgO [49]. Zero-point vibrational effects on the isothermal bulk modulus turn out to be remarkable, since K_T is lowered by ~ 5.5 GPa (i.e., $\sim 3.3\%$) with respect to the B3LYP static value (i.e., $K_0 = 167.01$ GPa). The zero-point correction effect on K_T is equal to $\sim 6\%$, $\sim 4.6\%$ and $\sim 2.3\%$ according to LDA [58], GGA [61] and hybrid WC1LYP [62] calculations, respectively (Table 1). K'_T increases with temperature and the temperature dependence predicted in this work is in good agreement both with LDA calculations [59] and thermodynamic assessments [63]. The effect of zero-point motions is again non-negligible, increasing the static value from 3.95 to 4.01 (Table 2). GGA calculations [61] are in good agreement with B3LYP at low temperatures, while they give lower values of K'_T in the medium- to high-temperature range.

Table 1. Ab initio B3LYP isothermal bulk modulus (K_T) of MgO. Values obtained in this work are compared to experiments [57] and other ab initio simulations at LDA [58,59] and GGA [61] level of theory.

T (K)	K_T (GPa) B3LYP	K_T (GPa) LDA [58]	K_T (GPa) LDA [59]	K_T (GPa) GGA [61]	K_T (GPa) Exp. [57]
$T = 0$ K	167.01 ¹ ; 161.53 ²	173 ¹ ; 164 ²	168.8 ²	181.24 ¹ ; 173.48 ²	-
$T = 300$ K	157.69	159	163.2	170.53	161.6 ± 0.6
$T = 1000$ K	138.38	139	143.0	152.59	141.4
$T = 2000$ K	107.78	108	114.9	127.72	110.7
$T = 3000$ K	74.26	74	86.7	106.11	-

¹ Static value; ² Value with zero-point correction (ZPC).

Table 2. Ab initio B3LYP temperature dependence of the isothermal bulk modulus pressure derivative (K'_T) of MgO. Values obtained in this work are compared to other ab initio simulations at LDA [59] and GGA [61] level of theory and thermodynamic assessment [63].

T (K)	K'_T (GPa) B3LYP	K'_T (GPa) LDA [59]	K'_T (GPa) GGA [61]	K_T (GPa) Assessment [63]
$T = 0$ K	3.95 ¹ ; 4.01 ²	-	3.997 ¹ ; 4.014 ²	-
$T = 300$ K	4.04	4.11	4.036	3.99
$T = 1000$ K	4.22	4.43	4.130	4.15
$T = 2000$ K	4.52	4.65	4.244	4.46
$T = 3000$ K	4.95	4.93	4.331	4.98

¹ Static value; ² Value with zero-point correction (ZPC).

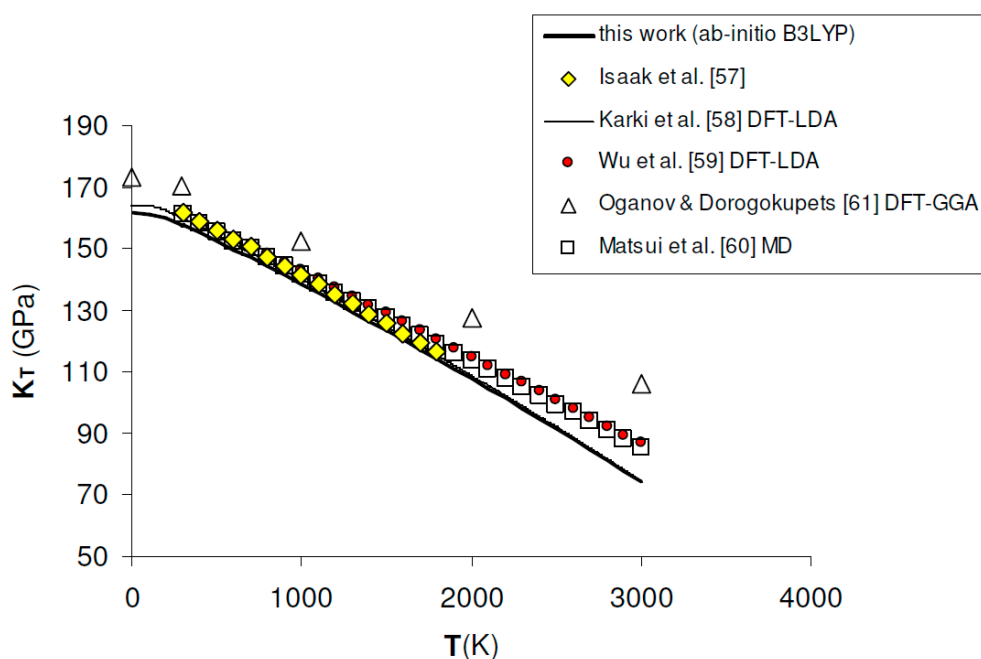


Figure 2. Ab initio B3LYP isothermal bulk modulus (K_T) of MgO. Calculated results in this work are compared to experimental data [57], other ab initio LDA [58,59] and GGA [61] calculations and semi-empirical MD simulation [60].

Thermal expansivity (α) can be simply obtained dividing out the values of the product αK_T by the values of K_T . In spite of the fact that B3LYP systematically overestimates molar volumes by $\sim 2\%$, the relative volume thermal expansion (i.e., V/V_0) and thermal expansivity (α) at discrete temperatures and ambient pressure are reproduced reasonably well up to $2/3$ of the melting temperature (i.e., $T \approx 2000$ K), then both start to deviate from the observed trend [49,64,65] (see Figures 3 and 4a). The agreement of ab initio B3LYP thermal expansivity with experimental data in the low-T range

(i.e., $T < 298.15$ K) [48,66] is excellent (see Figure 4b). The volume thermal expansion coefficient at ambient conditions as calculated in this work (i.e., $\alpha_0 = 2.97 \times 10^{-5} \text{ K}^{-1}$) fits well the experimental values, the latter being around $\alpha_0 = (3.12 \pm 0.16) \times 10^{-5} \text{ K}^{-1}$ [49,64–67]. The limit of QHA in reproducing thermal expansion at very high-temperature conditions is particularly evident in the values of α (Figure 4a); this is the reason that inflection points in the thermal expansivity function $\alpha = f(T)$ at various pressures have been considered by some authors to be a clue to empirically defining the P–T range of validity of QHA [68]. Nevertheless, it's interesting to note that B3LYP results show a less marked deviation in thermal expansivity at LP–HT with respect to those given by other density functionals (e.g., LDA) (see Figure 4a).

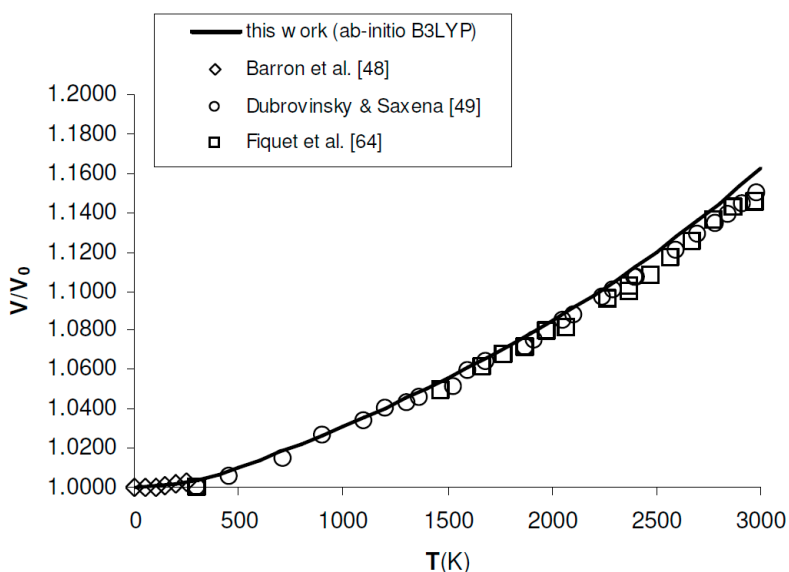


Figure 3. Ab initio B3LYP relative volume thermal expansion (V/V_0) of MgO, as compared to low-T to high-T experimental data [48,49,64]. Reference volume is $V_0 = 75.762 \text{ \AA}^3 = 11.406 \text{ cm}^3/\text{mol}$ ($T = 0$ K, $P = 0$ GPa, including ZPC).

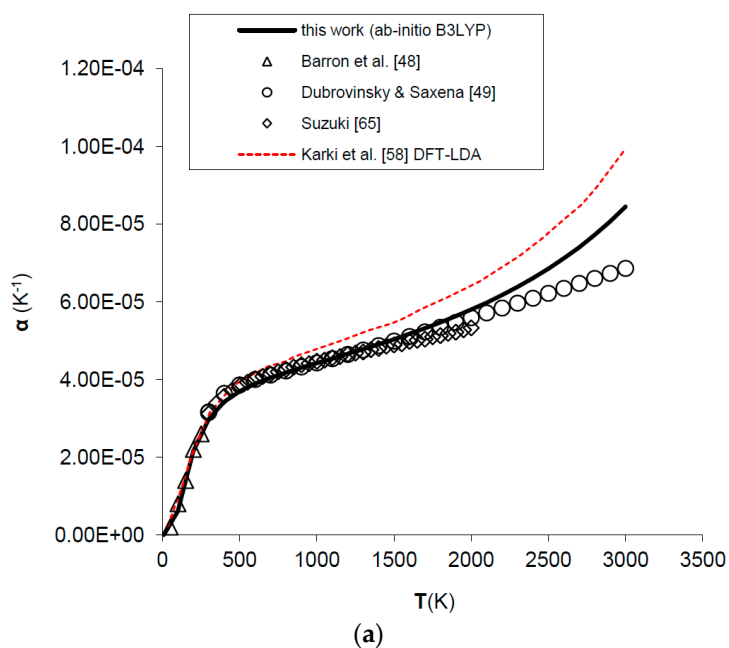


Figure 4. Cont.

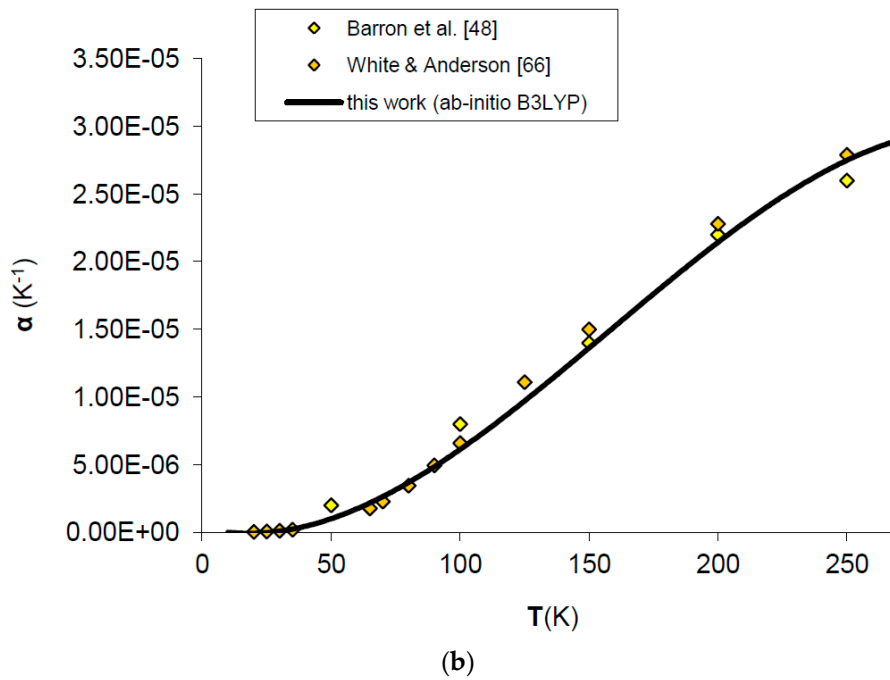


Figure 4. Ab initio B3LYP thermal expansivity (α) of MgO: calculated results in this work are compared to experimental data and other ab initio LDA calculations (a) in the whole T-range [48,49,58,65]; (b) in the low-T range [48,66].

3.2. Thermodynamic Properties

The calculation of vibrational frequencies (and phonon dispersion) in the harmonic approximation and the mode-gamma Grüneisen parameters in the QHA are the main ingredients also for the computation of thermodynamic properties. If insulating, ordered and stoichiometric crystalline solids (such as MgO) are taken into account, the vibrational contribution is only present in the general partition function [46]. The phonon contribution to the relevant thermodynamic properties, such as Hemholtz free energy (F_{vib}), internal energy (U_{vib}), isochoric heat capacity (C_V) and entropy (S_{vib}), can thus be determined according to Equation (1) (with ν_i calculated at different \mathbf{k} -points and different volumes) and to the following equations valid for the other thermodynamic functions:

$$U_{\text{vib}}(V, T) = \frac{RT}{Z} \sum_{i=1}^{3n} X_i(\vec{k}, V) \left(\frac{1}{2} + \frac{1}{e^{X_i(\vec{k}, V)} - 1} \right) = U_{\text{ZPC}}(V) + U_{\text{th}}(V, T) \quad (9)$$

$$C_V(V, T) = \frac{R}{Z} \sum_{i=1}^{3n} e^{X_i(\vec{k}, V)} \left(\frac{X_i(\vec{k}, V)}{e^{X_i(\vec{k}, V)} - 1} \right)^2 \quad (10)$$

$$S_{\text{vib}}(V, T) = \frac{R}{Z} \sum_{i=1}^{3n} \left(\frac{X_i(\vec{k}, V)}{e^{X_i(\vec{k}, V)} - 1} - \ln \left(1 - e^{-X_i(\vec{k}, V)} \right) \right) \quad (11)$$

Isobaric heat capacity (C_P) and total entropy (S) come out when the anharmonicity contribution is included in Equations (10) and (11), i.e.,

$$C_P(P, T) = C_V(V, T) + TV\alpha^2 K_T \quad (12)$$

$$S(P, T) = S_{\text{vib}}(V, T) + \int_0^T V\alpha^2 K_T dT \quad (13)$$

All the other thermodynamic functions (e.g., enthalpy, H ; Gibbs free energy, G ; etc.) can be derived from the fundamental thermodynamic relations [69].

Isobaric heat capacity (C_P) is a key thermodynamic property for testing the performance of hybrid DFT in predicting the thermodynamic properties of minerals, because *ab initio* results can be directly compared with calorimetric measurements in the low- T range and up to intermediate temperature conditions. Figure 5a shows the calculated results for C_P of MgO at low T (i.e., $T < 300$ K) as obtained by a phonon dispersion calculation with supercells of increasing size (i.e., $2 \times 2 \times 2$, $4 \times 4 \times 4$ and $5 \times 5 \times 5$). A few facts are noteworthy, when comparing *ab initio* B3LYP calculations with low- T calorimetric results [48]. First, a $2 \times 2 \times 2$ supercell calculation gives poor agreement with experimental data; this means that the phonon density of states (PDOS) is not adequately described in this case due to insufficient or overly coarse sampling of the reciprocal space. Second, numerical convergence for C_P is fulfilled after a $5 \times 5 \times 5$ supercell calculation (which corresponds to a 125 k -points sampling of the first BZ), since the difference between the calculated heat capacity values becomes negligible beyond this critical size. Finally, $5 \times 5 \times 5$ supercell calculations give an accuracy of $\sim 1\%$ or less in the simulation of the heat capacity and thermodynamic properties in the low- T range. This accuracy is well within the experimental uncertainty of current low- T relaxation calorimetry experiments [70–72].

Figure 5b shows as *ab initio* B3LYP phonon dispersion calculations are able to predict experimental C_P values determined by differential scanning calorimetry (DSC) [73] or assessed by thermodynamic tabulations (e.g., the NIST-JANAF, [74]); there is a good agreement up to roughly $T \approx 2000$ K, then deviations may occur, essentially due to the QHA overestimation of thermal expansivity (see Section 3.1). This holds also for B3LYP calculations, although the heat capacity overestimation seems to be lesser than that given by other density functionals [58]. The results obtained in the intermediate- to high-temperature range are summarized in Table 3. In this case, the difference between C_P values is relevant up to a $4 \times 4 \times 4$ supercell calculation, then becomes negligible because C_V tends to reach the Dulong-Petit limit (i.e., $3nR = 49.89$ J/mol \times K, where $n = 2$ is the number of atoms in the unit formula of MgO) and the anharmonic term (i.e., $TV\alpha^2K_T$) is less sensitive to k -point sampling.

Table 3. *Ab initio* B3LYP isobaric heat capacity (C_P) of MgO, as obtained in this work by phonon dispersion calculation with $2 \times 2 \times 2$, $4 \times 4 \times 4$ and $5 \times 5 \times 5$ supercells. Tabulated values by NIST-JANAF [74] are also shown for comparison.

T (K)	$2 \times 2 \times 2$ ab initio B3LYP	$4 \times 4 \times 4$ ab initio B3LYP	$5 \times 5 \times 5$ ab initio B3LYP	NIST-JANAF [74]
298.15	34.4	36.5	36.6	37.1
700	45.9	48.5	48.6	48.7
1000	48.5	51.1	51.3	51.2
1800	53.8	56.5	56.7	54.9

Entropy values (S) can be computed by Equations (11) and (13) and directly compared to those obtained by calorimetric measurements at ambient pressure. The standard-state entropy calculated in this work (i.e., $S_{298}^0 = 26.25$ J/mol·K) compares fairly well with the tabulated data (i.e., $S_{298}^0 = 26.924 \pm 0.08$ J/mol·K and $S_{298}^0 = 26.9 \pm 0.2$ J/mol·K according to [74,75], respectively). Most interestingly, $S_{\text{vib}}(V,T)$ or $S(P,T)$ can be computed in the whole P – T – V range of interest (i.e., up to lower mantle conditions) and compared to entropy values modelled from vibrational spectroscopy experiments [76] and thermodynamic assessments [50,77,78] (see Figure 6a,b). A decrease of entropy with pressure is obtained from first principles, i.e., $(\partial S/\partial P)_T < 0$ in the whole P – T range investigated in this work (0–160 GPa; 0–3000 K). This result has important implications for the P – V – T equation of state of periclase, as discussed below.

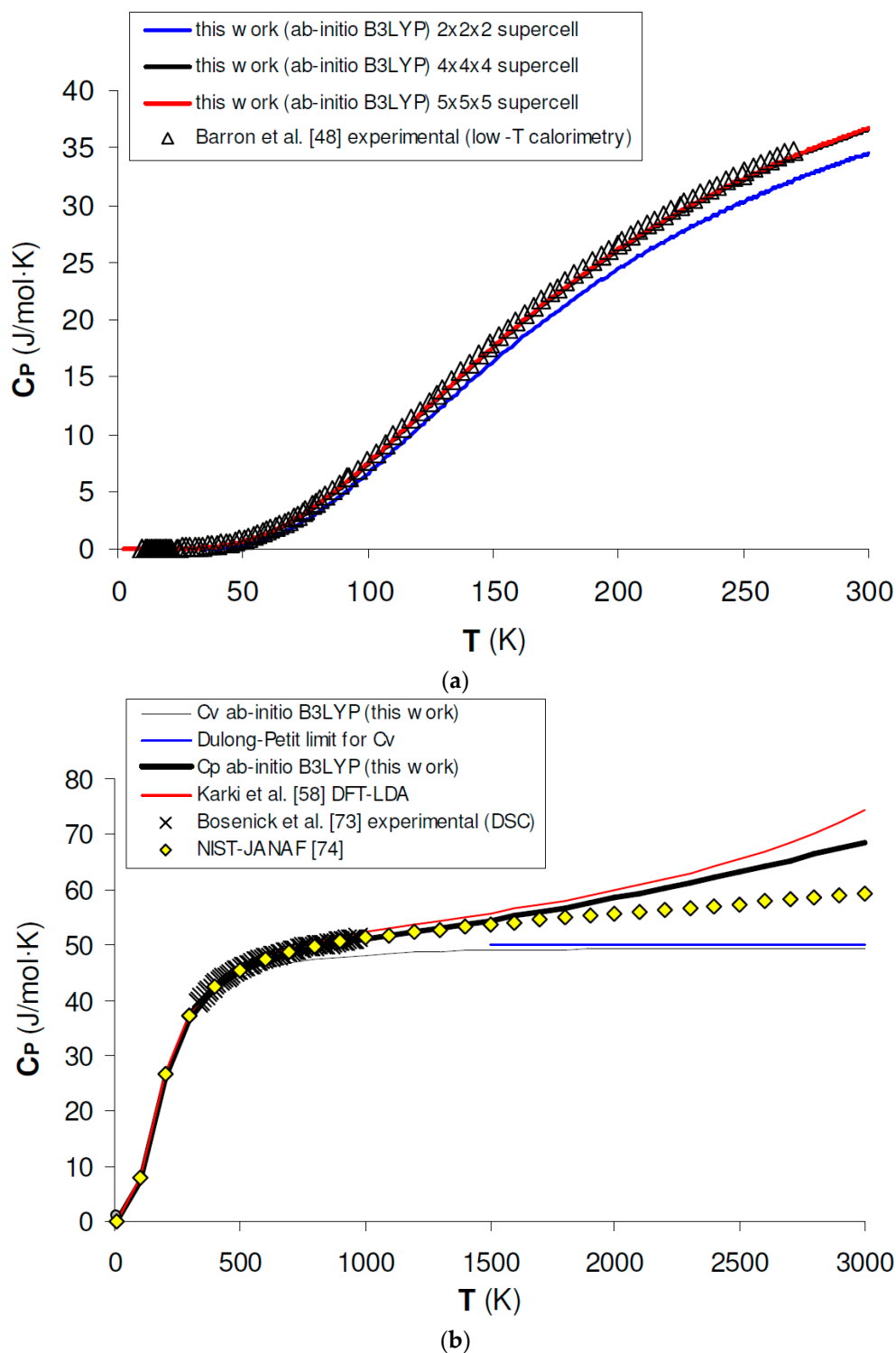


Figure 5. Ab initio B3LYP heat capacity (C_V , C_P) of MgO: (a) calculated results by phonon dispersion calculation with $2 \times 2 \times 2$, $4 \times 4 \times 4$ and $5 \times 5 \times 5$ supercells as compared to low-T calorimetry experimental data [48]; (b) calculated results in the whole T range as compared to experimental data by DSC [73], tabulated values by NIST-JANAF [74] and other ab initio LDA calculations [58].

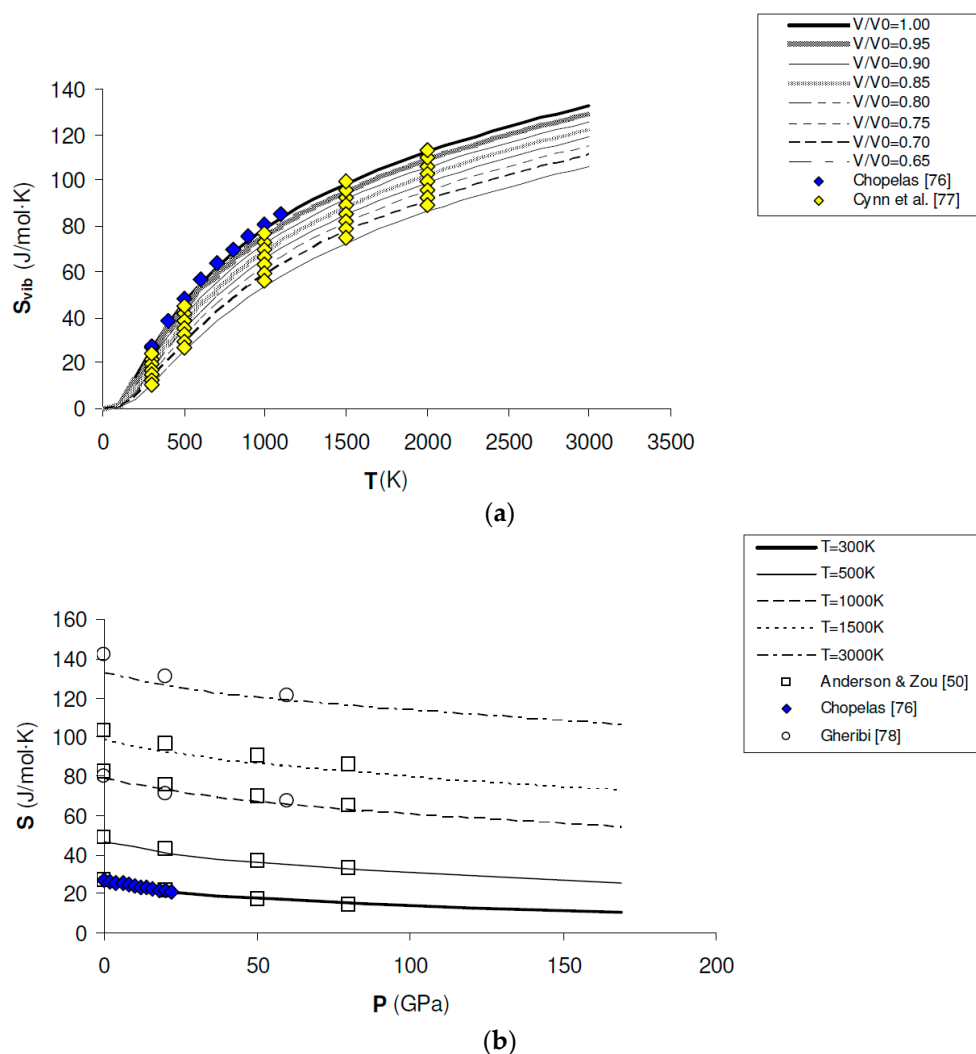


Figure 6. Ab initio B3LYP vibrational entropy (S_{vib}) and total entropy (S) of MgO: (a) calculated results along isochores (i.e., $V/V_0 = 0.65, 0.70, 0.75, 0.80, 0.95, 0.90, 0.95$ and 1.00), as compared to values modelled from vibrational spectroscopy experiments [76] and thermodynamic assessments [77]; (b) calculated results along isotherms (i.e., $T = 300\text{ K}, 500\text{ K}, 1000\text{ K}, 1500\text{ K}$ and 3000 K), as compared to values modelled from vibrational spectroscopy experiments [76] and thermodynamic assessments [50,78].

3.3. P – V – T Equation of State (EOS)

An equation of state (EOS) relates all the physical variables that control the free energy of a thermodynamic system, such as temperature (T), pressure (P) and volume (V). Since the nature of the equation of state is phenomenological—namely, intrinsically phase-dependent—there are plenty of formulations proposed in the literature (e.g., Murnaghan, Birch-Murnaghan, Vinet, natural strain, etc.), which rely on different theoretical assumptions [79–82]. MgO has always been a key phase for testing the performance of different EOS formalisms due to its simple structure and broad stability field [83–86]. Isothermal equations of state based on finite strain theory, like the third- or fourth-order Birch-Murnaghan EOS (BM3-EOS and BM4-EOS, respectively) [53], are among the most popular in the Earth Sciences, and have also been applied to high-temperature conditions (HT-BM-EOS) [2].

The Mie-Grüneisen equation of state (MG-EOS) [87] is perhaps the most straightforward way of describing the P – V – T relations of solids from first principles, as it is firmly grounded on the lattice dynamics theory of crystal lattices [88]. The MG-EOS formalism splits pressure into its different

contributions (namely static and vibrational, the latter being in turn split into zero-point correction and thermal contributions):

$$P(V, T) = - \left(\frac{\partial F}{\partial V} \right)_T = P_{\text{st}}(V) + P_{\text{vib}}(V, T) = P_{\text{st}}(V) + P_{\text{ZPC}}(V) + P_{\text{th}}(V, T) \quad (14)$$

In the statistical mechanics notation [46], Equation (14) can be restated as:

$$P(V, T) = - \left(\frac{\partial U_{\text{st}}}{\partial V} \right)_T + \frac{kT}{2V} \sum_{i=1}^{3n} \gamma_i(\vec{k}, V) X_i(\vec{k}, V) + \frac{kT}{V} \sum_{i=1}^{3n} \gamma_i(\vec{k}, V) \frac{X_i(\vec{k}, V)}{e^{X_i(\vec{k}, V)} - 1} \quad (15)$$

If vibrational frequencies at different volumes and mode-gamma Grüneisen parameters are available from ab initio phonon dispersion calculations), then a first principles Mie–Grüneisen equation of state (FPMG-EOS) will be obtained by plugging $X_i(\mathbf{k}, V)$ and $\gamma_i(\mathbf{k}, V)$ values into Equation (15).

Figure 7 and Table 4 show the results obtained for the P–V–T equation of state of periclase, as compared to different kinds of experimental data (i.e., static compression in the diamond-anvil cell, ultrasonic measurements, etc.) [89–97], semi-empirical modelling of experimental data [98–100] and other DFT [59,61,101] and MD [60,84] calculations. The EOS of MgO has been calculated according to Equation (15) in a range of conditions compatible with those realized in the Earth’s lower mantle (i.e., $P = 0\text{--}160$ GPa, $V/V_0 = 0.65\text{--}1.00$, $T = 0\text{--}3000$ K). Figure 7a displays the calculated results for the EOS at room temperature, and how the P–V–T relations of MgO are perfectly reproduced by means of a first principles Mie–Grüneisen formalism, whether including the zero-point correction term or not (dashed and bold curves in Figure 7a, respectively). It must be noted that ab initio calculations usually make a different choice of the reference state with respect to experimental measurements (i.e., $P = 0$ GPa, $T = 0$ K for the former; $P = 1$ bar, $T = 298.15$ K for the latter). The effect of the zero-point motions is to slightly raise the P–V–T curve. Ab initio P–V–T data are presented here without any further pressure correction. In other theoretical works, a pressure shift is applied to the calculated values to account for systematic errors of the density functional on volumes. Oganov and Dorogokupets [61], for instance, apply a pressure shift of about -7.7 GPa to the calculated static pressures to account for the systematic overestimation of lattice parameters by GGA ($\sim 1\text{--}2\%$) and to match the experimental unit cell volume in ambient conditions. Wu et al. [59] apply a more limited pressure correction to account for the systematic underestimation of volume by LDA ($\sim 0.6\%$) and to reproduce better the experimental results at LP conditions. Those corrections would be reasonable if the fundamental goal was the use of the first principles thermal EOS as a pressure scale (as in the case of MgO). However, even though B3LYP shares with other GGA functionals the same problem of volume overestimation ($\sim 2\text{--}3\%$, as already mentioned in Section 1), the aim of the present work is quite different, being the achievement of a first principles physically-consistent P–V–T dataset for the calculation of ΔG values of mineral reactions and the prediction of univariant phase equilibria at HP–HT conditions (see below). This is why theoretical results as directly provided by Equation (15) are considered throughout this work.

Raising the temperature doesn’t affect the accuracy of the simulation, which is still high and compares favorably with MD results [60,84] at selected high temperatures (i.e., $T = 1000$ K, 2000 K and 3000 K) and up to the melting point of the substance (see Figure 7b–d).

Thermal pressures (P_{th} in Equation (14)) calculated for MgO up to high volume compression (i.e., $V/V_0 = 0.70$) are compared with ambient-pressure experimental data [57] and a thermodynamic assessment [102] in Figure 8. Furthermore, the thermal pressure values estimated for the lower mantle by different geophysical models [103,104] are superimposed to the ab initio values of MgO. Some relevant considerations can be inferred from the analysis of Figure 8:

- (i) ab initio quasi-harmonic thermal pressure, in contrast to thermal expansivity, doesn’t display any deviation at $P = 0$ (i.e., $V/V_0 = 1.00$) and high-temperature conditions (i.e., $T > \Theta_D \cong 945$ K) (see also Section 3.1). This means that P_{th} is rather insensitive to QHA deviations at LP-HT

conditions, at least for what concerns the accuracy of numerical predictions, as already noted in other theoretical works [61,105,106]. Thermal pressure is quite insensitive to compression, too, especially in the low- to intermediate-T range;

- (ii) ab initio quasi-harmonic calculations of thermal pressure reproduce quite well the values assessed from experiments at 1-bar pressure [57,102]. The slight differences with respect to the values of Isaak et al. [57] and Srivastava [102] at low temperature are due to the constraint $P_{th}(300\text{ K}, 1\text{ bar}) = 0$, assumed to be valid in those works; this assumption lacks a theoretical justification, because thermal vibrations obviously occur already at $T = 0\text{ K}$ (zero-point motions), and their effects cannot be disregarded;
- (iii) Although the lower mantle consists primarily of bridgmanite, the thermal pressure of MgO seems to be representative of that of the lower mantle [103,104] owing to the peculiar thermoelastic and transport properties of periclase. Lower mantle thermodynamics and rheology are thus largely controlled by periclase and its Fe-bearing analogue (ferropericlase) [16,107–110].

Table 4. Ab initio B3LYP P–V–T EOS of MgO. Reference volume is $V_0 = 75.762\text{ \AA}^3$ ($T = 0\text{ K}$, $P = 0\text{ GPa}$).

V/V_0	T (K)	P_{st} (GPa) ¹	P_{ZPC} (GPa) ²	P_{th} (GPa) ²	P (GPa) ²
1.00	300	0.00	1.77	0.67	2.44
0.95	300	9.48	1.86	0.58	11.92
0.90	300	21.67	2.00	0.51	24.17
0.85	300	37.42	2.20	0.45	40.07
0.80	300	57.93	2.50	0.41	60.84
0.75	300	84.87	2.96	0.40	88.23
0.70	300	120.63	3.69	0.40	124.72
0.65	300	168.74	4.84	0.42	174.01
1.00	500	0.00	1.77	1.72	3.49
0.95	500	9.48	1.86	1.57	12.90
0.90	500	21.67	2.00	1.43	25.10
0.85	500	37.42	2.20	1.34	40.97
0.80	500	57.93	2.50	1.30	61.73
0.75	500	84.87	2.96	1.32	89.15
0.70	500	120.63	3.69	1.40	125.72
0.65	500	168.74	4.84	1.56	175.14
1.00	1000	0.00	1.77	4.70	6.47
0.95	1000	9.48	1.86	4.40	15.74
0.90	1000	21.67	2.00	4.19	27.85
0.85	1000	37.42	2.20	4.07	43.70
0.80	1000	57.93	2.50	4.11	64.54
0.75	1000	84.87	2.96	4.33	92.16
0.70	1000	120.63	3.69	4.80	129.11
0.65	1000	168.74	4.84	5.57	179.16
1.00	2000	0.00	1.77	10.90	12.67
0.95	2000	9.48	1.86	10.37	21.71
0.90	2000	21.67	2.00	10.02	33.68
0.85	2000	37.42	2.20	9.92	49.55
0.80	2000	57.93	2.50	10.20	70.63
0.75	2000	84.87	2.96	10.96	98.78
0.70	2000	120.63	3.69	12.380	136.69
0.65	2000	168.74	4.84	14.70	188.29
1.00	3000	0.00	1.77	17.16	18.93
0.95	3000	9.48	1.86	16.40	27.74
0.90	3000	21.67	2.00	15.92	39.59
0.85	3000	37.42	2.20	15.87	55.49
0.80	3000	57.93	2.50	16.40	76.83
0.75	3000	84.87	2.96	17.73	105.55
0.70	3000	120.63	3.69	20.16	144.47
0.65	3000	168.74	4.84	24.11	197.70

¹ Computed by fitting ab initio U_{st} -V data with BM3-EOS [53]; ² Computed by Equations (14) and (15).

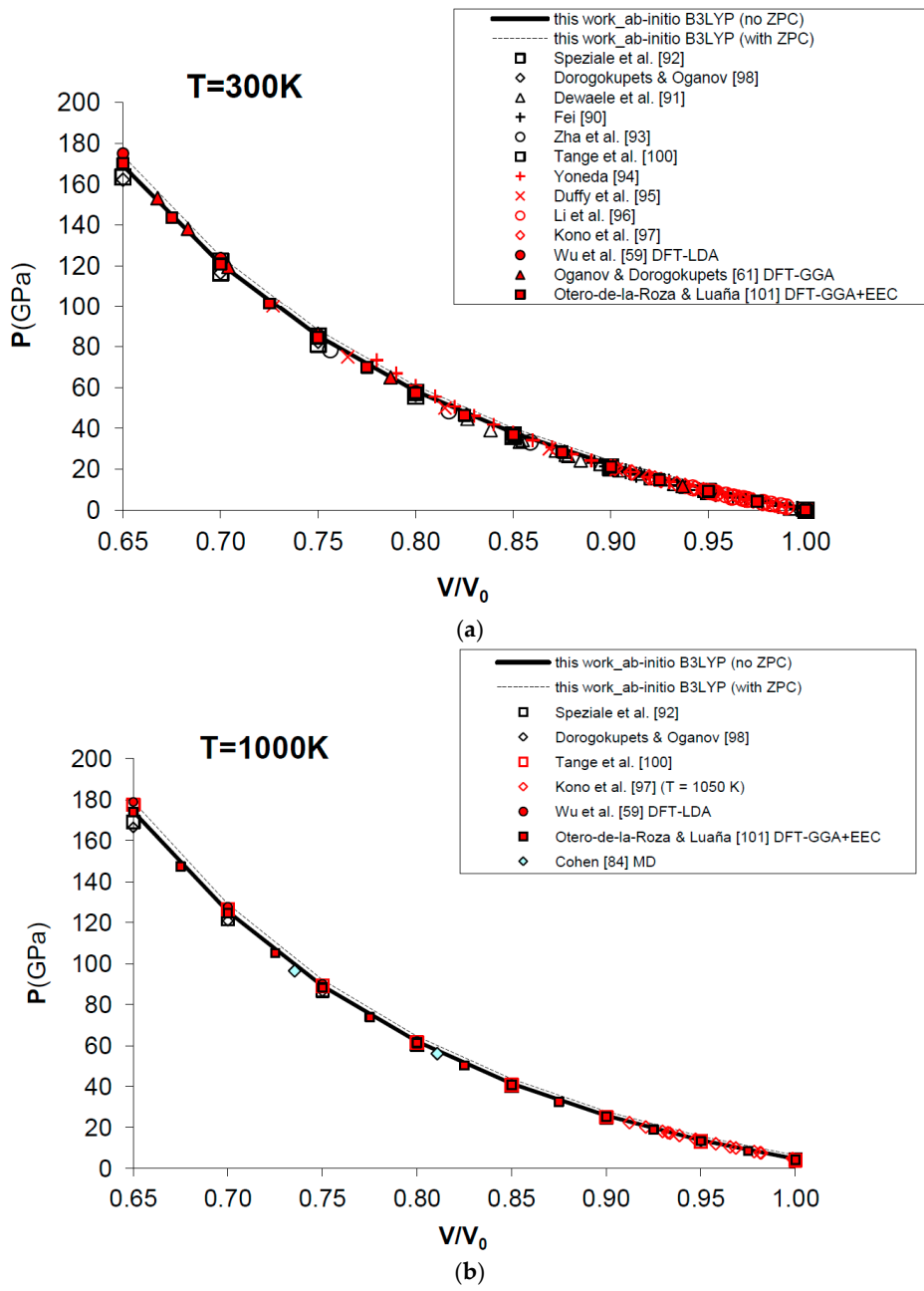


Figure 7. Cont.

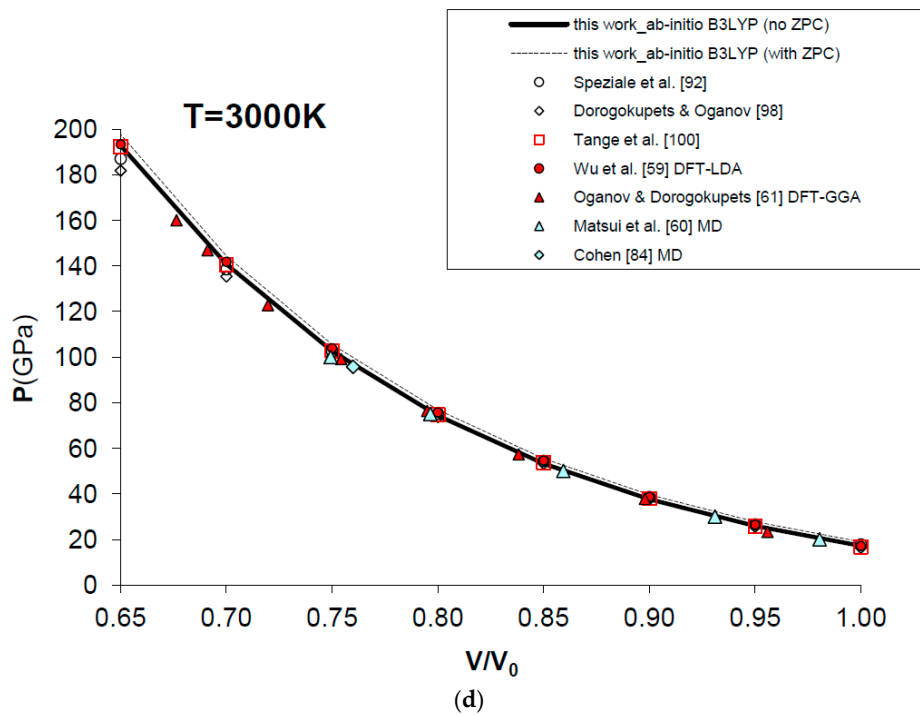
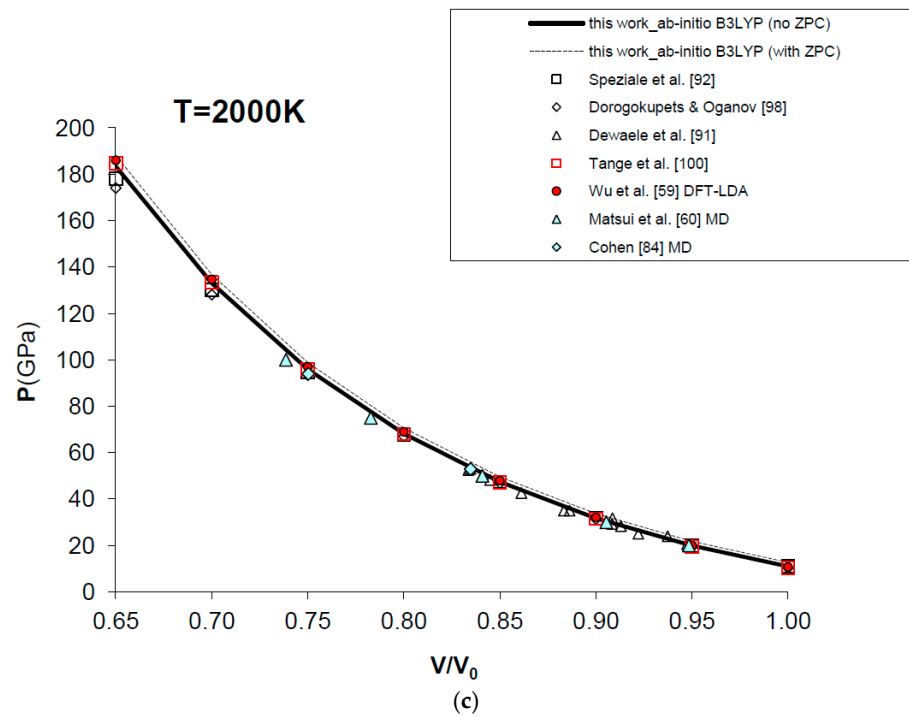


Figure 7. Cont.

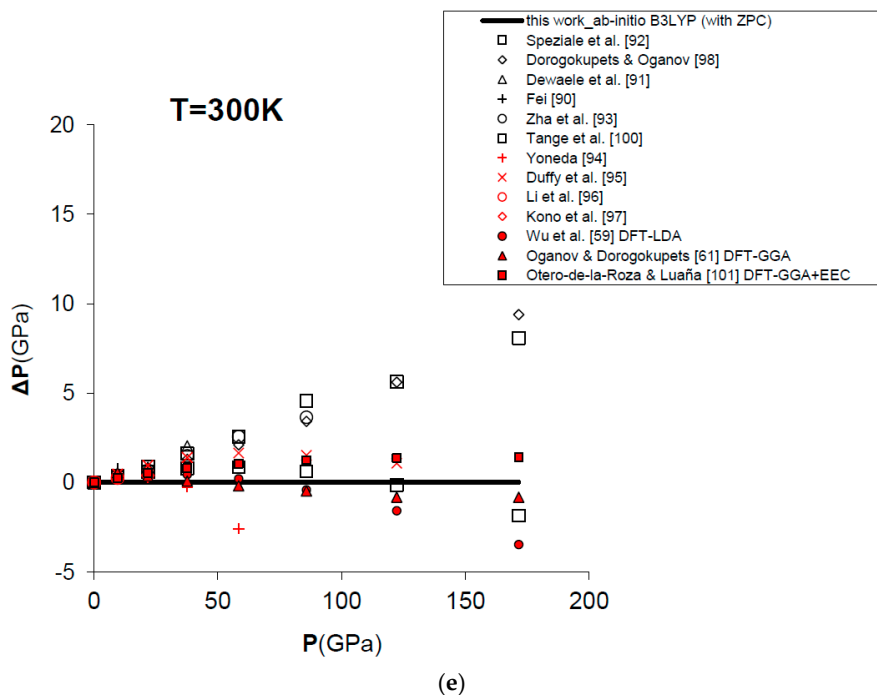


Figure 7. Ab initio B3LYP P–V–T equation of state (FPMG-EOS) of MgO, calculated with and without zero-point correction (ZPC) (dashed and bold curves, respectively; see Equations (14) and (15): (a) at T = 300 K; (b) at T = 1000 K; (c) at T = 2000 K; (d) at T = 3000 K; (e) deviation plot at T = 300 K. Calculated results of this work are compared to selected experimental data obtained by hydrostatic or quasi-hydrostatic compression in the diamond-anvil cell [90–93] and ultrasonic measurements [94–97]. The results of semi-empirical assessments [98,100], other ab initio LDA [59], GGA [61] and empirically-corrected GGA [101] calculations and MD simulations [60,84] are also shown for comparison.

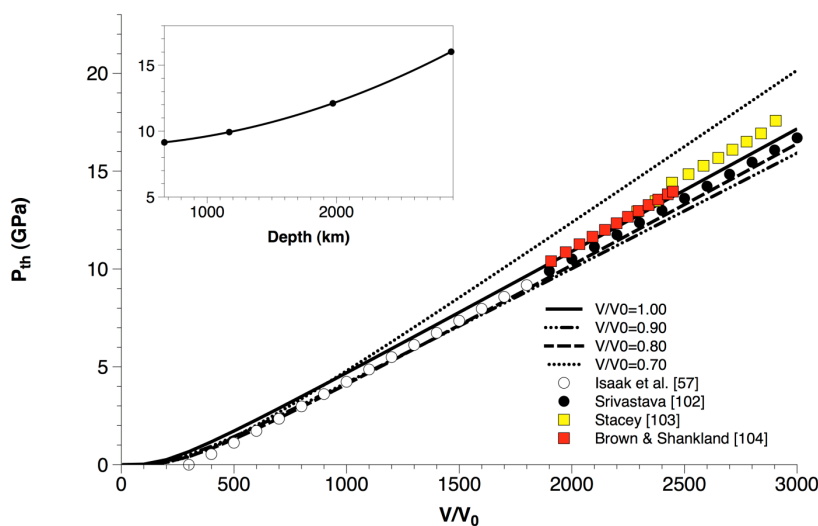


Figure 8. Ab initio B3LYP thermal pressure (P_{th}) calculated for MgO along different isochores and up to high volume compression (i.e., $V/V_0 = 0.70$), as compared to ambient-pressure experimental data [57] and a thermodynamic assessment [102]. The thermal pressure values estimated for the lower mantle by different geophysical models [103,104] are superimposed for comparison. The inset shows thermal pressure values calculated for MgO along a typical lower mantle geotherm taken from [104].

The most relevant thermophysical and thermodynamic functions calculated for MgO at $P = 1$ bar in the range $T = 298.15$ – 3000 K are listed in Appendix A (Table A1).

3.4. Phase Equilibrium Calculation at HP–HT: Modelling High-Pressure Effects on Gibbs Free Energy

Thermodynamic equilibrium of a reversible heterogeneous chemical reaction between fixed-composition (i.e., pure) phases at constant T, P is defined by the principle of Gibbs free energy minimization, i.e.,

$$\Delta G(T, P)_{\text{rxt}} = \Delta H(T, P_r)_{\text{rxt}} - T\Delta S(T, P_r)_{\text{rxt}} + \int_{P_r}^P \Delta V(T, P)_{\text{rxt}} dP = 0 \quad (16)$$

where ΔG_{xt} , ΔH_{rxt} , ΔS_{rxt} and ΔV_{rxt} are the Gibbs free energy, enthalpy, entropy and volume changes of the reaction, respectively; $P_r = 1$ bar is the standard-state reference pressure.

A straightforward way to define the phase equilibrium is to compute the Gibbs free energy of all the phases involved in the reaction at T, P in the so-called “explicit form” and then minimize ΔG of reaction at each T – P conditions according to the following equations:

$$G(T, P) = H_{298}^0 + \int_{T_r}^T C_p(T) dT - T \left(S_{298}^0 + \int_{T_r}^T \frac{C_p(T)}{T} dT \right) + \int_{P_r}^P V(T, P) dP \quad (17)$$

$$\Delta G(T, P)_{\text{rxt}} = \sum_i x_i G(T, P)_{\text{products, rxt}} - \sum_i x_i G(T, P)_{\text{reactants, rxt}} = 0 \quad (18)$$

where $T_r = 298.15$ K is the reference temperature; $H_{298}^0(T_r, P_r)$ is the standard-state enthalpy of the phase, which at T_r, P_r is equal to the enthalpy of formation from the elements at standard state (i.e., $H_{298}^0 = H_{f, 298}^0$ at T_r, P_r); $S_{298}^0(T_r, P_r)$ is the standard-state entropy; and x_i are the stoichiometric coefficients of the reactants and products in the reaction. In Equations (16)–(18) all thermodynamic entities refer to 1 mole of substance.

An alternative strategy for computing the Gibbs free energy of solid phases involved in the reaction is to define their Helmholtz free energy $F(V, T)$ and then the P – V contribution separately by operating a Legendre transformation (i.e., $G = F + PV$) [69]. The former can be derived directly from phonon dispersion calculations or, alternatively, by integrating the PDOS at the V, T conditions of interest (see Sections 3.1 and 3.2); the latter can be computed from the P – V – T curves which define the Mie–Grüneisen EOS of each phase (see Section 3.3). This procedure is formally correct and physically-consistent in the whole P – T – V range (see below), provided that a proper analytical description of the PDOS for all the phases involved in the equilibrium reaction is available from first principles. Phonon dispersion calculations, such as those presented in this work, are very labor intensive, so they might not be affordable for all the relevant mineralogical phases in thermodynamic databases. This is why Gibbs free energy minimization based on Equations (16)–(18) is usually performed at HP–HT [2].

The volume–pressure contribution to the Gibbs free energy is the key entity in phase equilibrium calculations at HP–HT [2,111]. Since pressure is experimentally easier than volume to keep constant in the solid state, the VdP integral in Equation (17) is commonly expressed as a PdV integral and calculated adopting an EOS formalism which relates the P – V – T variables. There are different analytical or numerical procedures to do this (see for instance [112] for details), but the most common way is to use a HT-BM3-EOS [2]. The great advantage in the use of finite strain EOSs to quantify pressure effects on the Gibbs free energy is that they require just ambient-pressure temperature-dependent thermophysical parameters (i.e., volume thermal expansion and isothermal compressibility) to calculate the $V(P, T)$ function. Nevertheless, it has been shown that HT-BM3-EOS is prone to giving spurious effects or anomalous predictions (i.e., negative thermal expansion) at very HP–HT conditions [63,113]. This has

led different authors to develop alternative formulations (more or less empirical) to describe the P–V–T relations of minerals up to planetary interior conditions [4,63,78,113–119]. Even though negative thermal expansion is obviously possible from a physical point of view as different minerals and compounds display a volume decrease with T not just in the low-P range [25,120], this phenomenon is systematically predicted by the HT-BM3-EOS at very HP–HT conditions. In particular, this usually happens beyond a threshold pressure which depends upon the thermophysical properties of the phase (and also on how these properties are defined), but it's typically around 25–30 GPa [63,113].

Figure 9 shows that using ab initio B3LYP thermophysical parameters (i.e., V_0 , K_0 , K'_0 , α , dK/dT) into a HT-BM3-EOS gives negative volume thermal expansion for MgO at $P = 160$ GPa (i.e., at conditions compatible with the base of the lower mantle), while the $V(P,T)$ function obtained by a FPMG-EOS (cf. Equation (15)) always has a positive slope over the whole P–T range, as expected for minerals with a close-packed B1-type structure. If the volume thermal expansion is negative, then entropy will increase with pressure by virtue of the Maxwell relation $(\partial S/\partial P)_T = -(\partial V/\partial T)_P$. This anomalous behavior, which for MgO occurs around 60 GPa, does not occur if lattice vibrations are properly taken into account in the P–V–T EOS, as done by the FPMG-EOS (see Figures 6b and 9). Therefore a HT-BM3-EOS (and other isothermal finite strain EOSs) should be used with care as P–V–T EOS at very HP–HT conditions, if the thermal or “hot” part of the EOS is not properly integrated with its compression or “cold” part.

Although a HT-BM3-EOS could give spurious predictions at very HP–HT conditions, it will not eventually affect the phase equilibrium calculation if the thermophysical properties of mineral phases involved in the equilibrium reaction are quite similar and differences among them thus cancel out [113]. A simple numerical exercise shows to what extent the adoption of a HT-BM3-EOS or a FPMG-EOS would affect the calculated values of Gibbs free energy of periclase at HP–HT conditions. The delta values calculated for the volume-pressure integral of MgO in Equation (17) by using the two equations of state are plotted against P and T in Figure 10. The difference turns out to be small (less than 1 kJ/mol) at LP–LT conditions but could sensibly increase (up to few tens of kJ/mol) at HP–HT, namely in the range of conditions where the HT-BM3-EOS could give numerical anomalies in the $V(P,T)$ values. Although there is nothing wrong with fitting P–V–T data with a finite strain EOS like the HT-BM3-EOS to extract thermophysical data such as K_T , K'_T , etc. (this is a common practice in both experimental and computational works, as already stressed in Section 3.1), it should be noted again that some care is required to avoid physical unsoundness, especially when those data are used to address the problem of phase stability at extreme conditions of P and T.

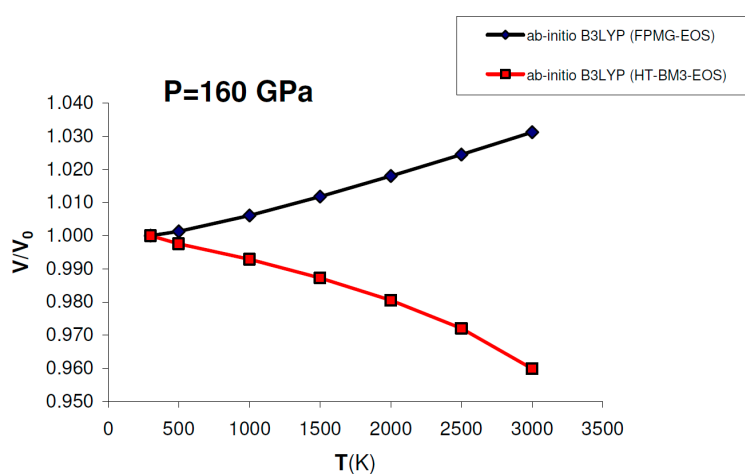


Figure 9. Ab initio B3LYP relative volume thermal expansion (V/V_0) of MgO calculated at $P = 160$ GPa by: (a) FPMG-EOS (blue) or (b) HT-BM3-EOS (red). While the former gives a $V/V_0 = f(T)$ function with a positive slope (i.e., positive thermal expansion) at $P = 160$ GPa, the latter gives an anomalous negative thermal expansion in the whole T-range at the same pressure (see text for discussion).

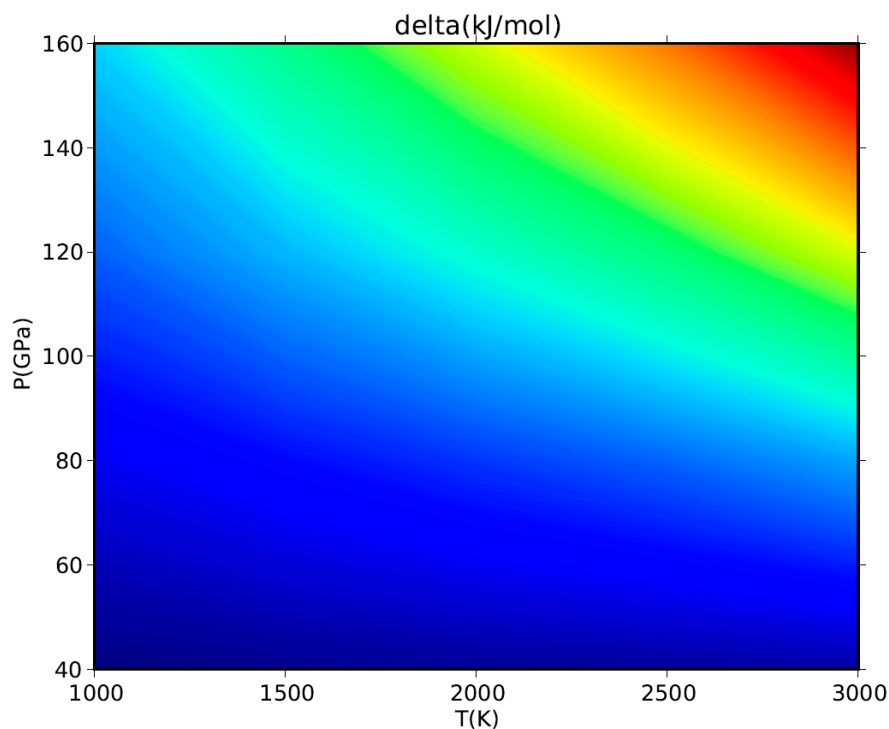


Figure 10. Effect of P–V–T EOS on the volume–pressure integral of MgO. Delta values of Gibbs free energy (in kJ/mol) calculated by using a HT-BM3-EOS or, alternatively, a FPMG-EOS for the volume–pressure integral (see Equation (17)) are plotted between $P = 40\text{--}160$ GPa and $T = 1000\text{--}3000$ K. Color scale as follows: blue = 6–30 kJ/mol; green = 30–45 kJ/mol, yellow = 45–50 kJ/mol, orange = 50–60 kJ/mol, red > 60 kJ/mol.

3.5. Phase Equilibrium Calculation at HP–HT: The Post-Spinel Phase Transformation

It is widely accepted that the disproportionation reaction of olivine with spinel-type structure (ringwoodite) into an assemblage of bridgmanite and ferropericlase (the so called “post-spinel phase transformation”) is an appropriate candidate to interpret the 660-km depth global seismic discontinuity in the Earth’s mantle [13,121,122]. For the magnesium end-member phases this reaction can be written as:



The post-spinel phase change turns out to be consistent with the 660-km mantle seismic discontinuity essentially because the stability field and seismic properties of minerals involved in the equilibrium reaction process are compatible with depth, density contrast and seismic velocity jumps associated with the discontinuity, as derived by seismological models (like the Preliminary Reference Earth Model, PREM) [123]. Owing to its geophysical implications, the Mg_2SiO_4 post-spinel phase transformations have been investigated by several experimental studies in the last decades [124–135]. Although experimental results are not consistent with each other concerning the P–T localization of the phase equilibrium boundary, there is general agreement about its most important thermodynamic feature; that is, the negative Clapeyron slope (i.e., $dP/dT < 0$) or endothermic character (i.e., $\Delta H_{\text{rxn}} > 0$). By virtue of the negative Clapeyron slope, this reaction may cause elevation and depression of the 660-km discontinuity within subducted slabs and the surrounding mantle due to lateral temperature variations, thus working as a potential barrier to the penetration of slabs beneath the mantle transition zone, and favoring stratified convection in the mantle [13].

The phase equilibrium boundary of post-spinel phase transformation calculated in this work from first principles is shown in Figure 11. Ab initio B3LYP thermodynamic data for Mg_2SiO_4 ringwoodite and MgSiO_3 bridgmanite have been taken from Ottonello et al. [36] and Belousov [136], respectively.

All the details about the calculation, along with a discussion on the possible effects of equation of state on the phase boundary, are given in Appendix B.

Ab initio B3LYP results show an excellent agreement with the in situ LH-DAC X-ray diffraction study of Shim et al. [128] and the multi-anvil experiments of Ishii et al. [132], as well as with calculations based on accurate calorimetric measurements by Akaogi and Ito [126] and Akaogi et al. [131] (Figure 11a; see also Figure A2 in Appendix B). This means that calculated values for ΔH_{298}^0 and ΔS_{298}^0 of the post-spinel reaction are consistent with those obtained by calorimetry (see Table 5), although a recent study found a lower enthalpy of reaction [134]. The ab initio phase boundary is localized at slightly higher pressures (≈ 1 – 2 GPa) than those determined by other HP–HT experiments [124,127,129,130,133] (see Figure 11a). The calculated Clapeyron slope (i.e., $dP/dT = -2.53$ MPa/K) agrees well with those obtained by the most part of experimental investigations (ranging from -4.0 to -2.0 MPa/K) [121,124–127,131,132,135], while other works [129,130,133,134] suggest a more gentle slope of the phase boundary (i.e., between -2.0 and -1.0 MPa/K or even less) (see Table 5). B3LYP results are in qualitative agreement with previous GGA calculations [137–139], whereas LDA [137] severely underestimates transformation pressures of the post-spinel reaction (see Figure 11b). However, ab initio Clapeyron slopes obtained by this and other DFT studies [137–139] seem to be consistent with each other, and less sensitive to the exchange-correlation term. The phase equilibrium boundary calculated in this work is also in good agreement with thermodynamic assessments based on lattice dynamical models [4,10,140]. The effect of lattice vibrations seems to be crucial to correctly predicting the high-pressure phase transformation; ab initio static enthalpy calculations [137–139,141] give transition pressures that are overestimated (by ≈ 1 – 2 up to 10 GPa) compared with those obtained by including vibrational contributions to thermodynamic properties (i.e., by minimizing Gibbs free energies instead of static enthalpies).

Table 5. Enthalpy (ΔH_{298}^0), entropy (ΔS_{298}^0) and volume change (ΔV_{298}^0) at $T = 298.15$ K, $P = 1$ bar and Clapeyron slope (dP/dT) of the post-spinel phase transformation (Equation (19)). Values obtained in this work are compared to experimental results [121,124–135] and other ab initio calculations [137–139].

Post-Spinel Reaction	ΔH_{298}^0 (kJ/mol)	ΔS_{298}^0 (J/mol·K)	ΔV_{298}^0 (cm ³ /mol)	dP/dT (MPa/K)
Ab initio (B3LYP, this work)	90.69	3.25	−3.52	−2.53
Exp. [125] (calorimetry)	96.8 ± 5.8	11.1 ± 3.7	-3.79 ± 0.04	-4.0 ± 2.0 ¹
Exp. [126] (calorimetry)	86.1 ± 3.6	1.2 ± 2.3	−3.84	-3.0 ± 1.0 ¹
Exp. [131] (calorimetry)	88.4 ± 2.5	1.4	−3.80	-2.6 ± 0.2 ¹
Exp. [134] (calorimetry)	78.54 ± 2.28	2.1 ± 0.6	−3.79	-1.5 ± 0.6 ¹
Exp. [135] (spectroscopy)	99.0 ²	9.5	−3.77	-2.5 ± 0.4
Exp. [121]	-	-	-	-2.3 ± 0.4 ¹
Exp. [124,127]	-	-	-	−2.8
Exp. [129]	-	-	-	-1.2 ± 0.8
Exp. [130]	-	-	-	-1.3 ± 0.3
Exp. [132]	-	-	-	−2.0
Exp. [133]	-	-	-	-0.55 ± 0.15
Ab initio (LDA/GGA) [137]	-	-	-	$-2.6/-2.9$
Ab initio (GGA) [138,139]	≈ 82 ³	3.78	−3.82	-3.9 ± 1.3

¹ Calculated value from calorimetric results; ² Assumed from calorimetry; ³ Static value (i.e., $T = 0$ K, $P = 0$ GPa).

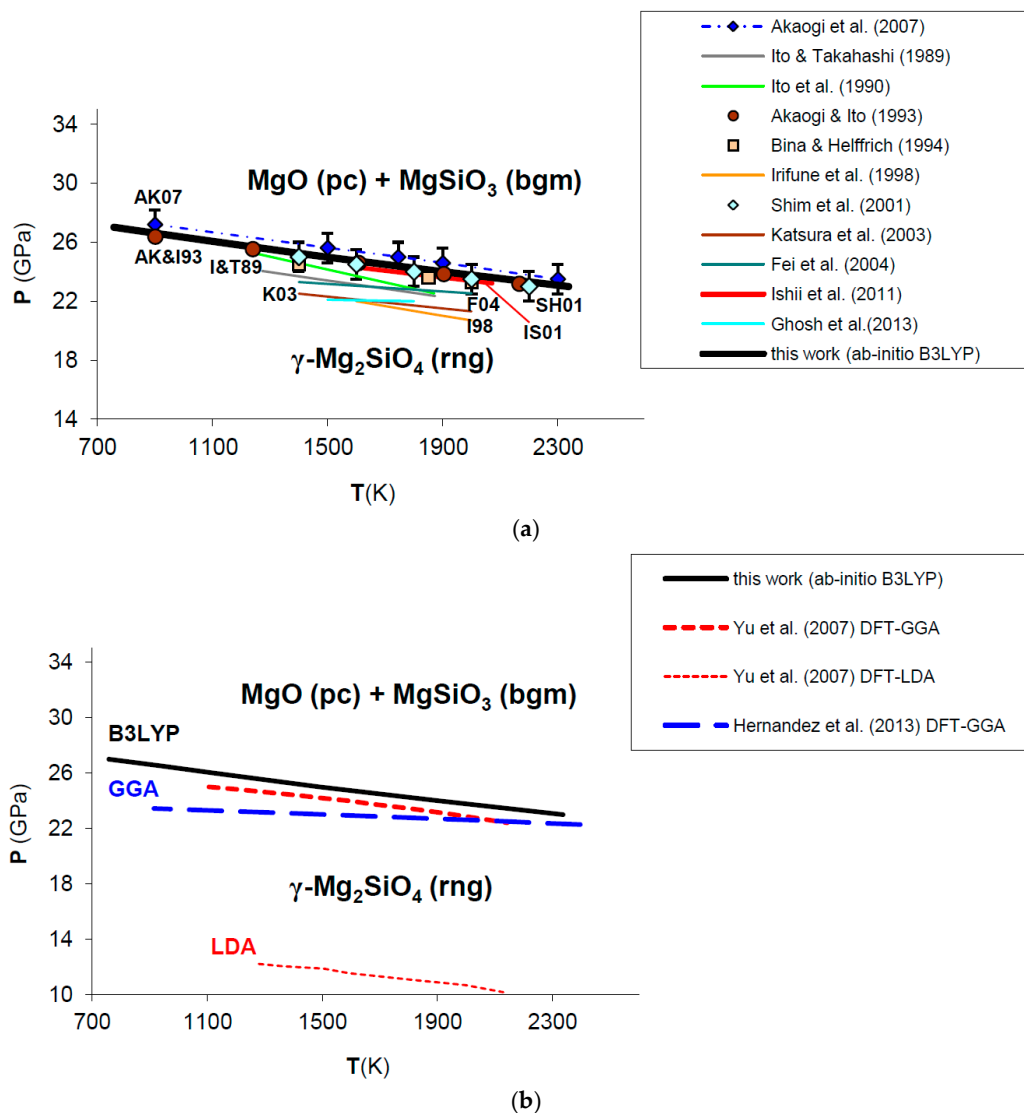


Figure 11. Ab initio B3LYP phase boundary of post-spinel transformation (in bold) as compared to: (a) experimental results (multi-anvil press, laser-heated diamond-anvil cell) [124,127–130,132,133] and calculations based on calorimetric measurements [121,125,126,131]; (b) other ab initio LDA [137] and GGA [138] calculations. Abbreviations for minerals are: rng = ringwoodite (γ -Mg₂SiO₄); pc = periclase (MgO); bgm = bridgmanite (MgSiO₃).

The density change of the post-spinel phase transformation provides useful insights on the interpretation of the 660-km seismic discontinuity in the Earth’s mantle. By assuming this discontinuity is produced primarily by the complete dissociation of Mg₂SiO₄ and the disproportionation reaction does not affect the stability of other mineralogical phases present in the Earth’s mantle at 660-km depths (such as majorite garnet and Ca-perovskite), the density change (i.e., $\Delta\rho/\rho$) of the post-spinel transformation (cf. Equation (19)) can be estimated as [137]:

$$\frac{\Delta\rho}{\rho}(T,P) = \frac{\rho_{pc+bgm,aggregate}(T,P) - \rho_{rng}(T,P)}{[\rho_{pc+bgm,aggregate}(T,P) + \rho_{rng}(T,P)]/2} \quad (20)$$

where ρ_{rng} and ρ_{pc+bgm} are the density of Mg₂SiO₄ ringwoodite (rng) and the average density of an isotropic aggregate of MgO periclase (pc) plus MgSiO₃ bridgmanite (bgm) at T,P of interest, respectively. Table 6 shows the results of the density change calculation at P–T conditions given by

the ab initio B3LYP phase boundary of Figure 11 and compatible with those of the Earth's mantle at 660-km depths [103,104,123], namely $P = 23\text{--}24$ GPa and $T = 1900\text{--}2337$ K. The calculated density jump across the 660-km discontinuity (i.e., 7.1–7.2%) turns out to be sensibly lower and higher, respectively, than those inferred by PREM [123] and the global seismic impedance study of Shearer and Flanagan [142]. This discrepancy can be interpreted in two alternative ways. If the 660-km seismic discontinuity were just due to the post-spinel phase transformation, the observed density jump would be reproduced only by assuming an incomplete dissociation reaction of ringwoodite in a mantle mineral aggregate; in fact, this would lead to an attenuation of the density change [137]. Alternatively, multiple reactions compatible with P–T conditions realized at the base of mantle transition zone (such as majorite garnet to bridgmanite phase transition, besides the post-spinel transformation) could occur simultaneously and could jointly contribute to determine the 660-km seismic discontinuity. This second scenario is nowadays supported by several evidences coming from seismology, geochemistry and mineral physics [122,143–148].

Table 6. Calculated density change ($\Delta\rho/\rho$; see Equation (20)) of the post-spinel phase transformation across the 660-km mantle seismic discontinuity, as compared to geophysical models [123,142]. The results of another DFT-GGA simulation [137] are also shown for comparison. Abbreviations for minerals are: rng = ringwoodite ($\gamma\text{-Mg}_2\text{SiO}_4$); pc = periclase (MgO); bgm = bridgmanite (MgSiO_3).

Density	This Work (Ab Initio B3LYP)	PREM [123]	SF'99 [142]	Yu07 [137]
ρ (g/cm ³) at depth < 660 km (rng)	3.70 ¹ 3.76 ²	3.99	-	3.81 ³
ρ (g/cm ³) at depth > 660 km (pc + bgm aggregate)	3.98 ¹ 4.04 ²	4.38	-	4.13 ³
$\Delta\rho/\rho$ (%) (rng → pc + pv)	7.1% ¹ 7.2% ²	9.3%	5 ± 1%	7.9% ³

¹ Calculated value at $P = 23$ GPa and $T = 2337$ K. ² Calculated value at $P = 24$ GPa and $T = 1900$ K. ³ Calculated value at $P = 23.2$ GPa and $T = 1900$ K.

4. Conclusions

The main conclusions of this work can be summarized as follows:

- At ambient pressure, ab initio thermophysical properties of MgO (such as α and K_T) show a good agreement with experimental data up to relatively high temperatures (i.e., $T \approx 1800\text{--}2000$ K), then deviations occur due to losing the power of the quasi-harmonic approximation at high-temperature (and low-pressure) conditions. Nevertheless, B3LYP results seem to show a less marked deviation in thermal expansivity with respect to other density functionals (e.g., LDA) under those conditions. Thermodynamic properties at low and up to relatively high temperatures are accurately defined by ab initio B3LYP phonon dispersion calculations. The level of accuracy with regard to current calorimetric results is around the experimental uncertainty (i.e., 1–2%) throughout the whole range of experimental measurement (i.e., $T = 298.15\text{--}1000$ K).
- A first principles Mie-Grüneisen EOS formalism (splitting pressure into static, zero-point and thermal contributions) gives reliable and physically-consistent P–V–T relations for MgO up to lower mantle conditions, provided that an accurate description of lattice vibrations and phonon density of state is available. Quasi-harmonic thermal pressures turn out to be rather insensitive to both volume compression and LP-HT deviations.
- P–V–T equations of state based on finite strain theory (such as HT-BM3-EOS) systematically predict anomalous thermodynamic functions (like negative thermal expansion or entropy increase with pressure) at HP–HT conditions. Nevertheless, spurious effects on the $V(P,T)$ function become relevant for MgO at pressures higher than 60 GPa, but in most cases don't have a huge impact

on phase equilibrium calculations at deep mantle conditions as the ensuing Gibbs free energy differences tend to cancel out.

- Hybrid DFT and statistical mechanics calculations in the quasi-harmonic approximation accurately simulate phase reaction boundaries, such as the post-spinel phase transformation of ringwoodite (Mg_2SiO_4) to periclase (MgO) and bridgmanite (MgSiO_3), at HP–HT conditions. Anharmonic effects, if any, are virtually irrelevant under those conditions. The hybrid B3LYP functional predicts accurate thermodynamic properties and, at the same time, reliable phase stability relations for magnesium oxide (and silicates) at HP–HT.
- The Clapeyron slope of post-spinel phase transformation is correctly predicted by ab initio B3LYP calculations, both in sign and magnitude. The calculated value in this work (i.e., $dP/dT = -2.53$ MPa/K) is in good agreement with the majority of experimental investigations, especially with those based on calorimetric measurements. Although the Clapeyron slope of the phase boundary is almost insensitive to the exchange-correlation term, its P–T location strongly depends upon the choice of the density functional: B3LYP results are in qualitative agreement with previous GGA calculations, while LDA drastically underestimates transformation pressures.
- The calculated density change across the post-spinel phase boundary at P–T conditions compatible with the 660-km seismic discontinuity in the Earth’s mantle is different from that inferred by geophysical models. This suggests either an incomplete dissociation reaction of ringwoodite to periclase + bridgmanite or the occurrence of multiple mineral phase changes in mantle aggregates at those depths.

Acknowledgments: This research was partially funded by the University of Genova (Fondo di Ricerca di Ateneo, Grant No. 100022-2015-FRA_Belmonte). The constructive remarks and comments of three anonymous reviewers are greatly appreciated. The author is grateful to Giulio Ottonello and Mauro Prencipe for critical reading of the manuscript and insightful discussions.

Conflicts of Interest: The author declares no conflict of interest.

Appendix A

Detailed tabulations of the most relevant thermophysical and thermodynamic properties calculated in this work for MgO (periclase, B1-type structure) are presented in Tables A1 and A2. The listed values refer to $P = 1$ bar and $T = 298.15$ – 3000 K.

Table A1. Ab initio B3LYP thermophysical and thermodynamic functions of MgO at P = 1 bar, T = 298.15–3000 K. Symbols: K_T = isothermal bulk modulus; α = thermal expansion coefficient (thermal expansivity); V_T = molar volume; C_V , C_P = isochoric and isobaric heat capacity; S = entropy; γ_{th} = Grüneisen thermodynamic parameter.

T (K)	K_T (GPa)	$\alpha \times 10^5$ (K ⁻¹)	V_T ¹ (cm ³ /mol)	C_V (J/mol·K)	C_P (J/mol·K)	S (J/mol·K)	γ_{th} ²
0	161.5	0.00	11.406	0.000	0.000	0.000	-
100	161.4	0.61	11.412	7.532	7.539	2.290	1.496
298.15	157.7	2.97	11.444	36.142	36.616	26.251	1.483
300	157.7	2.98	11.444	36.272	36.753	26.478	1.483
400	155.2	3.42	11.481	41.339	42.174	37.870	1.475
500	152.5	3.70	11.522	44.069	45.269	47.640	1.474
600	149.8	3.89	11.566	45.674	47.246	56.080	1.475
700	147.0	4.04	11.613	46.687	48.641	63.474	1.478
800	144.2	4.18	11.660	47.364	49.711	70.042	1.483
900	141.3	4.30	11.710	47.837	50.592	75.947	1.488
1000	138.4	4.42	11.760	48.180	51.361	81.314	1.493
1100	135.5	4.54	11.812	48.437	52.061	86.236	1.499
1200	132.5	4.66	11.866	48.633	52.724	90.787	1.505
1300	129.5	4.78	11.922	48.787	53.370	95.026	1.512
1400	126.5	4.90	11.979	48.910	54.010	98.999	1.519
1500	123.4	5.03	12.039	49.009	54.657	102.744	1.526
1600	120.4	5.17	12.100	49.090	55.320	106.293	1.534
1700	117.3	5.31	12.164	49.158	56.005	109.672	1.542
1800	114.1	5.47	12.231	49.215	56.719	112.902	1.550
1900	111.0	5.63	12.300	49.263	57.471	116.003	1.559
2000	107.8	5.80	12.372	49.304	58.265	118.988	1.568
2100	104.6	5.98	12.446	49.340	59.109	121.872	1.577
2200	101.3	6.17	12.524	49.371	60.011	124.665	1.587
2300	98.1	6.38	12.605	49.398	60.978	127.376	1.597
2400	94.8	6.61	12.688	49.421	62.020	130.013	1.607
2500	91.4	6.85	12.775	49.442	63.147	132.583	1.618
2600	88.1	7.12	12.865	49.461	64.374	135.093	1.630
2700	84.7	7.40	12.959	49.477	65.712	137.546	1.642
2800	81.2	7.72	13.056	49.492	67.180	139.947	1.654
2900	77.8	8.06	13.157	49.505	68.800	142.300	1.667
3000	74.3	8.45	13.262	49.517	70.594	144.608	1.680

¹ Calculated as $V_T = V_0 \exp \int \alpha(T) dT$ by fitting ab initio values of α with a polynomial function in T (i.e., $\alpha = \alpha_0 T + \alpha_1 + \alpha_2 T^{-1} + \alpha_3 T^{-2} + \alpha_4 T^{-3}$) (see also Appendix B).² Grüneisen parameter calculated as $\gamma_{th} = \alpha K_T V_T / C_V$ [47].

Table A2. Ab initio B3LYP vibrational contribution to thermodynamic functions of MgO at $P = 1$ bar, $T = 298.15$ – 3000 K. Symbols: U_{vib} = vibrational internal energy; H_{vib} = vibrational enthalpy; S_{vib} = vibrational entropy; F_{vib} , G_{vib} = vibrational Helmholtz and Gibbs free energy, respectively.

T (K)	U_{vib} (kJ/mol)	H_{vib} (kJ/mol)	S_{vib} (J/mol·K)	F_{vib} (kJ/mol)	G_{vib} (kJ/mol)
0	14.555 ¹	14.556	0.000	14.555	14.556
100	14.735	14.736	2.290	14.506	14.507
298.15	19.581	19.582	26.080	11.805	11.806
300	19.648	19.649	26.304	11.757	11.758
400	23.556	23.557	37.513	8.551	8.552
500	27.839	27.840	47.059	4.309	4.310
600	32.333	32.334	55.248	−0.816	−0.815
700	36.954	36.955	62.370	−6.705	−6.704
800	41.659	41.660	68.651	−13.262	−13.261
900	46.421	46.422	74.259	−20.412	−20.411
1000	51.222	51.223	79.318	−28.096	−28.095
1100	56.054	56.055	83.922	−36.261	−36.259
1200	60.908	60.909	88.146	−44.867	−44.866
1300	65.779	65.780	92.045	−53.879	−53.878
1400	70.664	70.665	95.665	−63.267	−63.266
1500	75.560	75.561	99.043	−73.004	−73.003
1600	80.465	80.466	102.208	−83.069	−83.067
1700	85.378	85.379	105.187	−93.439	−93.438
1800	90.296	90.297	107.998	−104.101	−104.099
1900	95.220	95.221	110.660	−115.035	−115.033
2000	100.149	100.150	113.188	−126.228	−126.226
2100	105.081	105.082	115.595	−137.668	−137.667
2200	110.017	110.018	117.891	−149.343	−149.341
2300	114.955	114.956	120.086	−161.243	−161.241
2400	119.896	119.897	122.189	−173.357	−173.356
2500	124.839	124.840	124.207	−185.678	−185.677
2600	129.784	129.785	126.146	−198.196	−198.195
2700	134.731	134.732	128.013	−210.905	−210.903
2800	139.680	139.681	129.813	−223.796	−223.795
2900	144.630	144.631	131.550	−236.865	−236.863
3000	149.581	149.582	133.228	−250.104	−250.103

¹ Zero-point correction to internal energy (i.e., U_{ZPC}).

Appendix B

The possible effects of the equation of state and thermodynamic parameters used for MgO on the post-spinel phase equilibrium boundary (cf. Equation (19)) are outlined in Figure A1.

The adoption of HT-BM3-EOS or FPMG-EOS to calculate the volume-pressure contribution to Gibbs free energy of MgO may alter the phase equilibrium boundary by ± 1 GPa (black and blue lines in Figure A1a, respectively). Actually, the effect of the EOS on the phase boundary is possibly less marked because P – V – T relations computed by FPMG-EOS (requiring a full ab initio B3LYP phonon dispersion calculation) are currently available for MgO (cf. Table 4 and Figure 7), but not yet for the other phases involved in the reaction (i.e., Mg_2SiO_4 ringwoodite and MgSiO_3 bridgmanite). It is sensible to assume that Gibbs free energy differences tend to cancel out and the computed phase boundaries to converge when the same EOS formalism (i.e., HT-BM3-EOS or FPMG-EOS) is used for all mineralogical phases of the reaction. Therefore the upper phase boundary (in blue in Figure A1a) is computed by using a HT-BM3-EOS for ringwoodite and bridgmanite and a FPMG-EOS for MgO according to the delta values calculated for the VdP integral in Figure 10 (see Section 3.4 for details). The lower phase boundary (in black in Figure A1b) is computed by the self-consistent use of HT-BM3-EOS for all phases in the reaction according to thermophysical properties listed in Table A3 (K_T , α and C_P polynomial functions are fitted to ab initio values). Enthalpy, entropy and volume changes of the reaction at $T = 298.15$ K,

$P = 1$ bar are obviously the same for both calculations (see Table 5). This exercise highlights that the effect of the EOS on the post-spinel phase boundary is virtually negligible at those P – T conditions. Furthermore, the phase boundary calculated by adopting a HT-BM3-EOS for all mineral phases is also physically sound in this case, because spurious effects on the $V(P,T)$ function of MgO becomes relevant at much higher pressures (i.e., $P > 60$ GPa).

Since the post-spinel reaction (cf. Equation (19)) is strongly volume-dependent, the effect of thermodynamic parameters on the phase equilibrium calculation has been tested by changing $\Delta V_{298,rx}^0$. Figure A1b shows two different phase boundaries computed by adopting either ab initio volumes (i.e., $\Delta V_{298,rx}^0 = -3.52$ cm³/mol; cf. Table 5) or experimental volumes ($\Delta V_{298,rx}^0 = -3.80$ cm³/mol) for periclase [49], bridgmanite [149] and ringwoodite [150] (black and blue lines in Figure A1b, respectively). It is quite evident from the analysis of Figure A1b that even small differences in volume may cause displacements of the phase boundary (~ 2 – 3 GPa in this case), which seem to be more relevant than those induced by the equation of state (see Figure A1a for comparison). The internal consistency of thermodynamic parameters (which is always ensured by first principles calculations) is thus crucial to accurately predicting phase equilibrium boundaries in HP–HT conditions.

Table A3. Ab initio B3LYP thermophysical properties used to calculate the post-spinel phase equilibrium (cf. Equation (19)). K_0 = bulk modulus at the athermal limit (i.e., $T = 0$ K, $P = 0$ GPa); $K'_0 = (dK/dP)_0$ = pressure derivative of the bulk modulus at $T = 0$ K, $P = 0$ GPa; $(dK/dT)_P$ = temperature derivative of the bulk modulus, with $K_T = K_0 + T \cdot (dK/dT)_P$; α = thermal expansivity (i.e., $\alpha = \alpha_0 T + \alpha_1 + \alpha_2 T^{-1} + \alpha_3 T^{-2} + \alpha_4 T^{-3}$); C_P = isobaric heat capacity (i.e., $C_P = a + bT + cT^{-2} + dT^2 + eT^{-0.5}$). Abbreviations for minerals as in Figure 11.

Thermophysical Properties	MgO (pc) ¹	MgSiO ₃ (bgm) ²	γ -Mg ₂ SiO ₄ (rng) ³
K_0 (GPa)	167.01	249.2	196.4
K'_0	3.95	4.2	4.322
$(dK/dT)_P$ (bar/K)	−308.0	−280.0	−104.108
$\alpha_0 \times 10^7$	0.2608	0.0818	0.0
$\alpha_1 \times 10^7$	−104.77954	198.2	323.0
$\alpha_2 \times 10^3$	42.9578	0.0	−7.3084
α_3	−17.04307	−0.474	1.3745
α_4	2122.59	0.0	−150.406
$a \times 10^{-2}$	0.44202	1.1012	1.5346
$b \times 10^2$	0.39852	0.95903	2.1405
$c \times 10^{-6}$	−1.2908	−3.8879	−4.749
$d \times 10^5$	0.12101	0.099651	−0.308
$e \times 10^{-2}$	0.93607	1.9259	1.2708

¹ This work; ² Belousov [136]; ³ Ottonello et al. [36].

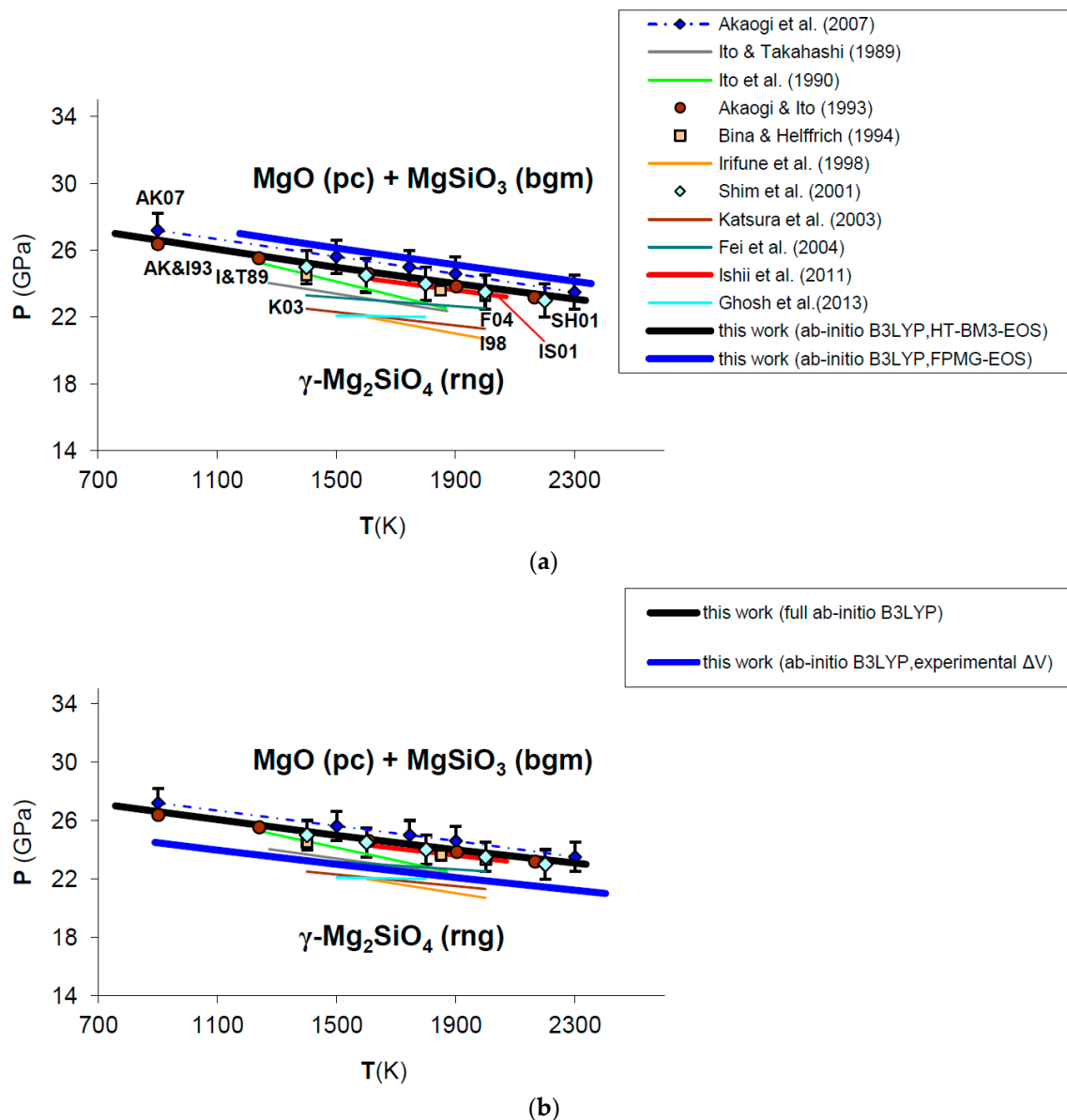


Figure A1. Effects of EOS and thermodynamic parameters on the post-spinel phase equilibrium: (a) ab initio B3LYP phase boundary calculated by adopting either a FPMG-EOS (blue line, in bold) or a HT-BM3-EOS (black line, in bold) for MgO; (b) ab initio B3LYP phase boundary calculated by adopting either ab initio volumes (black line, in bold) or experimental volumes (blue line, in bold) for all phases in the reaction. Experimental results are shown for comparison (cf. Figure 11). Abbreviations for minerals and labels as in Figure 11.

A detailed comparison between the post-spinel phase boundary calculated ab initio in this work and selected experimental results obtained in the laser-heated diamond-anvil cell [128] or multi-anvil apparatus [132] is shown in Figure A2. Linear best-fits of experimental runs are also indicated (red and blue lines in Figure A2a,b, respectively).

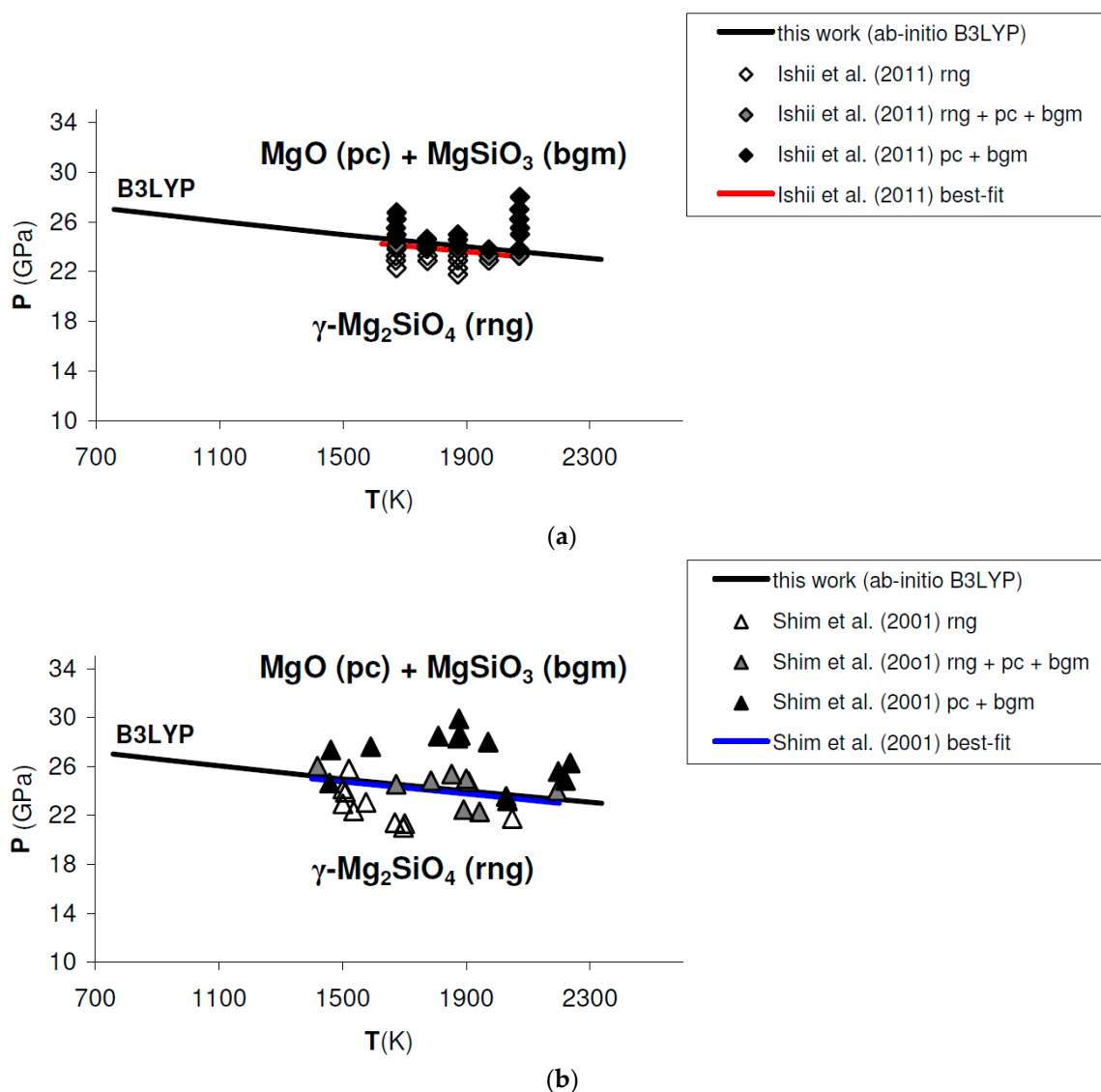


Figure A2. Ab initio B3LYP phase boundary of post-spinel transformation (in bold) as compared to: (a) results obtained by multi-anvil experiments (diamonds) [132]; (b) results obtained by laser-heated diamond-anvil cell experiments (triangles) [128]. Best-fits of experimental results are also indicated. Abbreviations for minerals as in Figure 11.

References

1. Kuskov, O.L.; Fabrichnaya, O.B. Constitution of the Moon: 1. Composition and seismic properties of the lower mantle. *Phys. Earth Planet. Inter.* **1994**, *83*, 197–216. [[CrossRef](#)]
2. Saxena, S.K. Earth mineralogical model: Gibbs free energy minimization computation in the system MgO-FeO-SiO₂. *Geochim. Cosmochim. Acta* **1996**, *60*, 2379–2395. [[CrossRef](#)]
3. Bina, C.R. Free energy minimization by simulated annealing with applications to lithospheric slabs and mantle plumes. *Pure Appl. Geophys.* **1998**, *151*, 605–618. [[CrossRef](#)]
4. Jacobs, M.H.G.; de Jong, B.H.W.S. Placing constraints on phase equilibria and thermophysical properties in the system MgO-SiO₂ by a thermodynamically consistent vibrational method. *Geochim. Cosmochim. Acta* **2007**, *71*, 3630–3655. [[CrossRef](#)]
5. Piazzoni, A.S.; Steinle-Neumann, G.; Bunge, H.-P.; Dolejš, D. A mineralogical model for density and elasticity of the Earth's mantle. *Geochem. Geophys. Geosyst.* **2007**, *8*, Q11010. [[CrossRef](#)]

6. Ganguly, J.; Freed, A.M.; Saxena, S.K. Density profiles of oceanic slabs and surrounding mantle: Integrated thermodynamic and thermal modelling, and implications for the fate of slabs at the 660 km discontinuity. *Phys. Earth Planet. Inter.* **2009**, *172*, 257–267. [[CrossRef](#)]
7. Khan, A.; Connolly, J.A.D.; Olsen, N. Constraining the composition and thermal state of the mantle beneath Europe from inversion of long-period electromagnetic sounding data. *J. Geophys. Res. Solid Earth* **2006**, *111*, B10102. [[CrossRef](#)]
8. Connolly, J.A.D.; Khan, A. Uncertainty of mantle geophysical properties computed from phase equilibrium models. *Geophys. Res. Lett.* **2016**, *43*, 5026–5034. [[CrossRef](#)]
9. Stixrude, L.; Lithgow-Bertelloni, C. Thermodynamics of mantle minerals—I. Physical properties. *Geophys. J. Int.* **2005**, *162*, 610–632. [[CrossRef](#)]
10. Stixrude, L.; Lithgow-Bertelloni, C. Thermodynamics of mantle minerals—II. Phase equilibria. *Geophys. J. Int.* **2011**, *184*, 1180–1213. [[CrossRef](#)]
11. Belmonte, D.; Ottonello, G.; Vetuschi Zuccolini, M.; Attene, M. The system MgO-Al₂O₃-SiO₂ under pressure: A computational study of melting relations and phase diagrams. *Chem. Geol.* **2017**, *461*, 54–64. [[CrossRef](#)]
12. Belmonte, D.; Ottonello, G.; Vetuschi Zuccolini, M. Ab initio-assisted assessment of the CaO-SiO₂ system under pressure. *Calphad* **2017**, *59*, 12–30. [[CrossRef](#)]
13. Christensen, U. Effects of phase transitions on mantle convection. *Annu. Rev. Earth Planet. Sci.* **1995**, *23*, 65–87. [[CrossRef](#)]
14. Faccenda, M.; Dal Zilio, L. The role of solid-solid phase transitions in mantle convection. *Lithos* **2017**, *268*, 198–224. [[CrossRef](#)]
15. Bina, C.R. Lower mantle mineralogy and the geophysical perspective. In *Ultrahigh-Pressure Mineralogy: Physics and Chemistry of the Earth's Deep Interior. Reviews in Mineralogy*; Hemley, R.J., Ed.; Mineralogical Society of America: Chantilly, VA, USA, 1998; Volume 37, pp. 205–240.
16. Yamazaki, D.; Karato, S.-I. Some mineral physics constraints on the rheology and geothermal structure of Earth's lower mantle. *Am. Mineral.* **2001**, *86*, 385–391. [[CrossRef](#)]
17. Karki, B.B.; Stixrude, L.; Clark, S.J.; Warren, M.C.; Ackland, G.J.; Crain, J. Structure and elasticity of MgO at high pressure. *Am. Mineral.* **1997**, *82*, 51–60. [[CrossRef](#)]
18. Tsuchiya, T.; Kawamura, K. Systematics of elasticity: Ab initio study in B1-type alkaline earth oxides. *J. Chem. Phys.* **2001**, *114*, 10086–10093. [[CrossRef](#)]
19. Wentzcovitch, R.M.; Wu, Z.; Carrier, P. First principles quasiharmonic thermoelasticity of mantle minerals. In *Theoretical and Computational Methods in Mineral Physics: Geophysical Applications. Reviews in Mineralogy and Geochemistry*; Wentzcovitch, R.M., Stixrude, L., Eds.; Mineralogical Society of America and Geochemical Society: Chantilly, VA, USA, 2010; Volume 71, pp. 99–128.
20. Becke, A.D. Density-functional thermochemistry. III. The role of exact exchange. *J. Chem. Phys.* **1993**, *98*, 5648–5652. [[CrossRef](#)]
21. Demichelis, R.; Civalleri, B.; Ferrabone, M.; Dovesi, R. On the performance of eleven DFT functionals in the description of the vibrational properties of aluminosilicates. *Int. J. Quantum Chem.* **2010**, *110*, 406–415. [[CrossRef](#)]
22. Demichelis, R.; Civalleri, B.; D'Arco, P.; Dovesi, R. Performance of 12 DFT functionals in the study of crystal systems: Al₂SiO₅ orthosilicates and Al hydroxides as a case study. *Int. J. Quantum Chem.* **2010**, *110*, 2260–2273. [[CrossRef](#)]
23. De La Pierre, M.; Orlando, R.; Maschio, L.; Doll, K.; Ugliengo, P.; Dovesi, R. Performance of six functionals (LDA, PBE, PBESOL, B3LYP, PBE0 and WC1LYP) in the simulation of vibrational and dielectric properties of crystalline compounds. The case of forsterite Mg₂SiO₄. *J. Comput. Chem.* **2011**, *32*, 1775–1784. [[CrossRef](#)] [[PubMed](#)]
24. De La Pierre, M.; Belmonte, D. Ab initio investigation of majorite and pyrope garnets: Lattice dynamics and vibrational spectra. *Am. Mineral.* **2016**, *101*, 162–174. [[CrossRef](#)]
25. Prencipe, M.; Mantovani, L.; Tribaudino, M.; Bersani, D.; Lottici, P.P. The Raman spectrum of diopside: A comparison between ab initio calculated and experimentally measured frequencies. *Eur. J. Mineral.* **2012**, *24*, 457–464. [[CrossRef](#)]
26. Prencipe, M.; Scanavino, I.; Nestola, F.; Merlini, M.; Civalleri, B.; Bruno, M.; Dovesi, R. High-pressure thermo-elastic properties of beryl (Al₄Be₆Si₁₂O₃₆) from ab initio calculations, and observations about the source of thermal expansion. *Phys. Chem. Miner.* **2011**, *38*, 223–239. [[CrossRef](#)]

27. Zucchini, A.; Prencipe, M.; Belmonte, D.; Comodi, P. Ab initio study of the dolomite to dolomite-II high-pressure phase transition. *Eur. J. Mineral.* **2017**, *29*, 227–238. [[CrossRef](#)]
28. Ottonello, G.; Civalleri, B.; Ganguly, J.; Perger, W.F.; Belmonte, D.; Vetuschi Zuccolini, M. Thermo-chemical and thermo-physical properties of the high-pressure phase anhydrous B ($\text{Mg}_{14}\text{Si}_5\text{O}_{24}$): An ab-initio all-electron investigation. *Am. Mineral.* **2010**, *95*, 563–573. [[CrossRef](#)]
29. Ottonello, G.; Vetuschi Zuccolini, M.; Belmonte, D. The vibrational behavior of silica clusters at the glass transition: Ab initio calculations and thermodynamic implications. *J. Chem. Phys.* **2010**, *133*, 104508. [[CrossRef](#)] [[PubMed](#)]
30. Belmonte, D.; Ottonello, G.; Vetuschi Zuccolini, M. Melting of $\alpha\text{-Al}_2\text{O}_3$ and vitrification of the undercooled alumina liquid: Ab initio vibrational calculations and their thermodynamic implications. *J. Chem. Phys.* **2013**, *138*, 064507. [[CrossRef](#)] [[PubMed](#)]
31. Belmonte, D.; Ottonello, G.; Vetuschi Zuccolini, M. Ab initio thermodynamic and thermophysical properties of sapphirine end-members in the join $\text{Mg}_4\text{Al}_8\text{Si}_2\text{O}_{20}\text{-Mg}_3\text{Al}_{10}\text{SiO}_{20}$. *Am. Mineral.* **2014**, *99*, 1449–1461. [[CrossRef](#)]
32. Belmonte, D.; Gatti, C.; Ottonello, G.; Richet, P.; Vetuschi Zuccolini, M. Ab initio thermodynamic and thermophysical properties of sodium metasilicate, Na_2SiO_3 , and their electron-density and electron-pair-density counterparts. *J. Phys. Chem. A* **2016**, *120*, 8881–8895. [[CrossRef](#)] [[PubMed](#)]
33. Erba, A.; Mahmoud, A.; Belmonte, D.; Dovesi, R. High pressure elastic properties of minerals from ab initio simulations: The case of pyrope, grossular and andradite silicate garnets. *J. Chem. Phys.* **2014**, *140*, 124703. [[CrossRef](#)] [[PubMed](#)]
34. Kohanoff, J. *Electronic Structure Calculations for Solids and Molecules: Theory and Computational Methods*; Cambridge University Press: Cambridge, UK, 2006; p. 372.
35. Corà, F.; Alfredsson, M.; Mallia, G.; Middlemiss, D.S.; Mackrodt, W.C.; Dovesi, R.; Orlando, R. The Performance of Hybrid Density Functionals in Solid State Chemistry. In *Structure and Bonding, Principles and Applications of Density Functional Theory in Inorganic Chemistry II*; Kaltsoyannis, N., McGrady, J.E., Eds.; Springer: Berlin/Heidelberg, Germany, 2004; Volume 113, pp. 171–232.
36. Ottonello, G.; Civalleri, B.; Ganguly, J.; Vetuschi Zuccolini, M.; Noël, Y. Thermophysical properties of the $\alpha\text{-}\beta\text{-}\gamma$ polymorphs of Mg_2SiO_4 : A computational study. *Phys. Chem. Miner.* **2009**, *36*, 87–106. [[CrossRef](#)]
37. Dovesi, R.; Saunders, V.R.; Roetti, C.; Orlando, R.; Zicovich-Wilson, C.M.; Pascale, F.; Civalleri, B.; Doll, K.; Harrison, N.M.; Bush, I.J.; et al. *CRYSTAL14 User's Manual*; Università di Torino: Torino, Italy, 2014; 382p.
38. Lee, C.; Yang, E.; Parr, R.G. Development of the Colle-Salvetti correlation-energy formula into a functional of the electron density. *Phys. Rev. B* **1988**, *37*, 785–789. [[CrossRef](#)]
39. Monkhorst, H.J.; Pack, J.D. Special points for Brillouin-zone integrations. *Phys. Rev. B* **1976**, *13*, 5188–5192. [[CrossRef](#)]
40. Broyden, C.G. The converge of a class of double-rank minimization algorithms 1. General considerations. *IMA J. Appl. Math.* **1970**, *6*, 76–90. [[CrossRef](#)]
41. Civalleri, B.; D'Arco, P.; Orlando, R.; Saunders, V.R.; Dovesi, R. Hartree-Fock geometry optimization of periodic system with the CRYSTAL code. *Chem. Phys. Lett.* **2001**, *348*, 131–138. [[CrossRef](#)]
42. Doll, K. Implementation of analytical Hartree-Fock gradients for periodic systems. *Comput. Phys. Commun.* **2001**, *137*, 74–88. [[CrossRef](#)]
43. Pascale, F.; Zicovich-Wilson, C.M.; López Gejo, F.; Civalleri, B.; Orlando, R.; Dovesi, R. The calculation of the vibrational frequencies of crystalline compounds and its implementation in the CRYSTAL code. *J. Comput. Chem.* **2004**, *25*, 888–895. [[CrossRef](#)] [[PubMed](#)]
44. Parlinski, K.; Li, Z.Q.; Kawazoe, Y. First-principles determination of the soft mode in cubic ZrO_2 . *Phys. Rev. Lett.* **1997**, *78*, 4063–4066. [[CrossRef](#)]
45. Alfè, D. PHON: A program to calculate phonons using the small displacement method. *Comput. Phys. Commun.* **2009**, *180*, 2622–2633. [[CrossRef](#)]
46. Landau, L.D.; Lifshitz, E.M. *Statistical Physics. Part 1*, 3rd ed.; Butterworth-Heinemann: Oxford, UK, 1980; pp. 191–224.
47. Anderson, O.L. *Equation of State for Geophysics and Ceramic Science. Oxford Monographs on Geology and Geophysics*; Oxford University Press: New York, NY, USA, 1995; Volume 31, pp. 3–18.
48. Barron, T.H.K.; Berg, W.T.; Morrison, J.A. On the heat capacity of crystalline magnesium oxide. *Proc. R. Soc.* **1959**, *250*, 70–83. [[CrossRef](#)]

49. Dubrovinsky, L.S.; Saxena, S.K. Thermal expansion of periclase (MgO) and tungsten (W) to melting temperatures. *Phys. Chem. Miner.* **1997**, *24*, 547–550. [[CrossRef](#)]
50. Anderson, O.L.; Zou, K. Thermodynamic functions and properties of MgO at high compression and high temperature. *J. Phys. Chem. Ref. Data* **1990**, *19*, 69–81. [[CrossRef](#)]
51. Singh, B.P.; Srivastava, S.K.; Dinesh, K. Relation between thermal expansivity and bulk modulus for ionic solids at high temperatures. *Phys. B* **2004**, *349*, 401–407. [[CrossRef](#)]
52. Pavese, A. Pressure-volume-temperature equations of state: A comparative study based on numerical simulations. *Phys. Chem. Miner.* **2002**, *29*, 43–51. [[CrossRef](#)]
53. Angel, R.J. Equations of state. In *High-Temperature and High-Pressure Crystal Chemistry. Reviews in Mineralogy and Geochemistry*; Hazen, R.M., Downs, R.T., Eds.; Mineralogical Society of America and Geochemical Society: Chantilly, VA, USA, 2000; Volume 41, pp. 35–60.
54. Angel, R.J.; Gonzalez-Platas, J.; Alvaro, M. EosFit7c and a Fortran module (library) for equation of state calculations. *Z. Krist.* **2014**, *229*, 405–419. [[CrossRef](#)]
55. Duffy, T.S.; Wang, Y. Pressure-volume-temperature equations of state. In *Ultra-high-Pressure Mineralogy: Physics and Chemistry of the Earth's Deep Interior. Reviews in Mineralogy*; Hemley, R.J., Ed.; Mineralogical Society of America: Chantilly, VA, USA, 1998; Volume 37, pp. 425–457.
56. Oganov, A.R.; Brodholt, J.P.; Price, G.D. Ab initio theory of phase transitions and thermoelasticity of minerals. In *Energy Modelling in Minerals. EMU Notes in Mineralogy*; Gramaccioli, C.M., Ed.; Eötvös University Press: Budapest, Hungary, 2002; Volume 4, pp. 83–170.
57. Isaak, D.G.; Anderson, O.L.; Goto, T. Measured elastic moduli of single-crystal MgO up to 1800 K. *Phys. Chem. Miner.* **1989**, *16*, 704–713. [[CrossRef](#)]
58. Karki, B.B.; Wentzcovitch, R.M.; de Gironcoli, S.; Baroni, S. High-pressure lattice dynamics and thermoelasticity of MgO. *Phys. Rev. B* **2000**, *61*, 8793–8800. [[CrossRef](#)]
59. Wu, Z.; Wentzcovitch, R.M.; Umemoto, K.; Li, B.; Hirose, K.; Zheng, J.-C. Pressure-volume-temperature relations in MgO: An ultrahigh pressure-temperature scale for planetary sciences applications. *J. Geophys. Res. Solid Earth* **2008**, *113*, B06204. [[CrossRef](#)]
60. Matsui, M.; Parker, S.C.; Leslie, M. The MD simulation of the equation of state of MgO: Application as a pressure calibration standard at high temperature and high pressure. *Am. Mineral.* **2000**, *85*, 312–316. [[CrossRef](#)]
61. Oganov, A.R.; Dorogokupets, P.I. All-electron and pseudopotential study of MgO: Equation of state, anharmonicity, and stability. *Phys. Rev. B* **2003**, *67*, 224110. [[CrossRef](#)]
62. Scanavino, I.; Belousov, R.; Prencipe, M. Ab initio quantum-mechanical study of the effects of the inclusion of iron on thermoelastic and thermodynamic properties of periclase (MgO). *Phys. Chem. Miner.* **2012**, *39*, 649–663. [[CrossRef](#)]
63. Jacobs, M.H.G.; Oonk, H.A.J. A realistic equation of state for solids. The high pressure and high temperature thermodynamic properties of MgO. *Calphad* **2000**, *24*, 133–147. [[CrossRef](#)]
64. Fiquet, G.; Richet, P.; Montagnac, G. High-temperature thermal expansion of lime, periclase, corundum and spinel. *Phys. Chem. Miner.* **1999**, *27*, 103–111. [[CrossRef](#)]
65. Suzuki, I. Thermal expansion of periclase and olivine, and their anharmonic properties. *J. Phys. Earth* **1975**, *23*, 145–159. [[CrossRef](#)]
66. White, G.K.; Anderson, O.L. Gruneisen parameter of magnesium oxide. *J. Appl. Phys.* **1966**, *37*, 430–432. [[CrossRef](#)]
67. Touloukian, Y.S.; Kirby, R.K.; Taylor, R.E.; Lee, T.Y.R. *Thermal Expansion: Nonmetallic Solids. Thermophysical Properties of Matter*, 1st ed.; IFI/Plenum: New York, NY, USA, 1977; Volume 13, p. 1786.
68. Wentzcovitch, R.M.; Yu, Y.G.; Wu, Z. Thermodynamic properties and phase relations in mantle minerals investigated by first principles quasiharmonic theory. In *Theoretical and Computational Methods in Mineral Physics: Geophysical Applications. Reviews in Mineralogy and Geochemistry*; Wentzcovitch, R.M., Stixrude, L., Eds.; Mineralogical Society of America and Geochemical Society: Chantilly, VA, USA, 2010; Volume 71, pp. 59–98.
69. Callen, H.B. *Thermodynamics*, 1st ed.; John Wiley & Sons, Inc.: New York, NY, USA, 1960; pp. 85–102.
70. Lashley, J.C.; Hundley, M.F.; Migliori, A.; Sarrao, J.L.; Pagliuso, P.G.; Darling, T.W.; Jaime, M.; Cooley, J.C.; Hulth, W.L.; Morales, L.; et al. Critical examination of heat capacity measurements made on a Quantum Design physical property measurement system. *Cryogenics* **2003**, *43*, 369–378. [[CrossRef](#)]

71. Dachs, E.; Bertoldi, C. Precision and accuracy of the heat-pulse calorimetric technique: Low-temperature heat capacities of milligram-sized synthetic mineral samples. *Eur. J. Mineral.* **2005**, *17*, 251–261. [[CrossRef](#)]
72. Dachs, E.; Benisek, A. A sample-saving method for heat capacity measurements on powders using relaxation calorimetry. *Cryogenics* **2011**, *51*, 460–464. [[CrossRef](#)] [[PubMed](#)]
73. Bosenick, A.; Geiger, C.; Cemič, L. Heat capacity measurements of synthetic pyrope-grossular garnets between 320 and 1000 K by differential scanning calorimetry. *Geochim. Cosmochim. Acta* **1996**, *60*, 3215–3227. [[CrossRef](#)]
74. Chase, M.W., Jr. *NIST-JANAF Thermochemical Tables. Journal of Physical and Chemical Reference Data, Monograph No. 9, Part II. Cr-Zr*, 4th ed.; American Chemical Society and American Institute of Physics for the National Institute of Standards and Technology: New York, NY, USA, 1998; pp. 1536–1538.
75. Robie, R.A.; Hemingway, B.S. *Thermodynamic Properties of Minerals and Related Substances at 298.15 K and 1 Bar (10⁵ Pascals) Pressures and at Higher Temperatures*, U.S. Geological Survey Bulletin 2131; U.S. Geological Survey: Denver, Colorado, VA, USA, 1995; p. 197.
76. Chopelas, A. Thermal expansion, heat capacity, and entropy of MgO at mantle pressures. *Phys. Chem. Miner.* **2000**, *17*, 142–148. [[CrossRef](#)]
77. Cynn, H.; Anderson, O.L.; Isaak, D.G.; Nicol, M. Grüneisen ratio of MgO from the calculation of entropy. *J. Phys. Chem.* **1995**, *99*, 7813–7818. [[CrossRef](#)]
78. Gheribi, A.E. Formulation of the thermal volume consistent with Swenson's concept of thermal pressure. *Phys. Earth Planet. Inter.* **2009**, *177*, 59–64. [[CrossRef](#)]
79. Murnaghan, F.D. Finite deformations of an elastic solid. *Am. J. Math.* **1937**, *49*, 235–260. [[CrossRef](#)]
80. Birch, F. Finite elastic strain of cubic crystals. *Phys. Rev. Lett.* **1947**, *71*, 809–824. [[CrossRef](#)]
81. Vinet, P.; Ferrante, J.; Smith, J.R.; Rose, J.H. A universal equation of state for solids. *J. Phys. C Solid State Phys.* **1986**, *19*, L467–L473. [[CrossRef](#)]
82. Poirier, J.-P.; Tarantola, A. A logarithmic equation of state. *Phys. Earth Planet. Inter.* **1998**, *109*, 1–8. [[CrossRef](#)]
83. Hama, J.; Suito, K. The search for a universal equation of state correct up to very high pressures. *J. Phys. Condens. Matter* **1996**, *8*, 67–81. [[CrossRef](#)]
84. Cohen, R.E. MgO—The simplest oxide. In *Physics Meets Mineralogy: Condensed-Matter Physics in Geosciences*; Aoki, H., Syono, Y., Hemley, R.J., Eds.; Cambridge University Press: Cambridge, UK, 2000; pp. 95–123.
85. Ponkratz, U.; Holzapfel, W.B. Equations of state for wide ranges in pressure and temperature. *J. Phys. Condens. Matter* **2004**, *16*, S963–S972. [[CrossRef](#)]
86. Bose Roy, P.; Bose Roy, S. Applicability of isothermal three-parameter equations of state of solids—A reappraisal. *J. Phys. Condens. Matter* **2005**, *17*, 6193–6216.
87. Grüneisen, E. Zustand de festen Körpers. In *Thermische Eigenschaften der Stoffe*; Springer: Berlin/Heidelberg, Germany, 1926; Volume 10, pp. 1–59.
88. Born, M.; Huang, K. *Dynamical Theory of Crystal Lattices*, 1st ed.; Oxford University Press: London, UK, 1954; pp. 38–128.
89. Utsumi, W.; Weidner, D.J.; Liebermann, R.C. Volume measurement of MgO at high pressures and high temperatures. In *Properties of Earth and Planetary Materials at High Pressure and Temperature. Geophysical Monograph Series*; Manghnani, M.H., Yagi, T., Eds.; American Geophysical Union: Washington, DC, USA, 1998; Volume 101, pp. 327–333.
90. Fei, Y. Effects of temperature and composition on the bulk modulus of (Mg,Fe)O. *Am. Mineral.* **1999**, *84*, 272–276. [[CrossRef](#)]
91. Dewaele, A.; Fiquet, G.; Andrault, D.; Hausermann, D. P–V–T equation of state of periclase from synchrotron radiation measurements. *J. Geophys. Res. Solid Earth* **2000**, *105*, 2869–2877. [[CrossRef](#)]
92. Speziale, S.; Zha, C.-S.; Duffy, T.S.; Hemley, R.J.; Mao, H. Quasi-hydrostatic compression of magnesium oxide to 52 GPa: Implications for the pressure-volume-temperature equation of state. *J. Geophys. Res. Solid Earth* **2001**, *106*, 515–528. [[CrossRef](#)]
93. Zha, C.-S.; Mibe, K.; Bassett, W.A.; Tschauer, O.; Mao, H.; Hemley, R.J. P–V–T equation of state of platinum to 80 GPa and 1900 K from internal resistive heating/X-ray diffraction measurements. *J. Appl. Phys.* **2008**, *103*, 054908. [[CrossRef](#)]
94. Yoneda, A. Pressure derivatives of elastic constants of single crystal MgO and MgAl₂O₄. *J. Phys. Earth* **1990**, *38*, 19–55. [[CrossRef](#)]

95. Duffy, T.S.; Hemley, R.J.; Mao, H. Equation of state and shear strength at multimegabar pressures: Magnesium oxide to 227 GPa. *Phys. Rev. Lett.* **1995**, *74*, 1371–1374. [[CrossRef](#)] [[PubMed](#)]
96. Li, B.; Woody, K.; Kung, J. Elasticity of MgO to 11 GPa with an independent absolute pressure scale: Implications for pressure calibration. *J. Geophys. Res. Solid Earth* **2006**, *111*, B11206. [[CrossRef](#)]
97. Kono, Y.; Irifune, T.; Higo, Y.; Inoue, T.; Barnhoorn, A. P–V–T relations of MgO derived by simultaneous elastic wave velocity and in situ X-ray measurements: A new pressure scale for the mantle transition region. *Phys. Earth Planet. Int.* **2010**, *183*, 196–211. [[CrossRef](#)]
98. Dorogokupets, P.I.; Oganov, A.R. Ruby, metals, and MgO as alternative pressure scales: A semiempirical description of shock-wave, ultrasonic, X-ray, and thermochemical data at high temperatures and pressures. *Phys. Rev. B* **2007**, *75*, 024115. [[CrossRef](#)]
99. Garai, J.; Chen, J.; Telekes, G. The P–V–T equation of state of periclase. *Calphad* **2009**, *33*, 737–743. [[CrossRef](#)]
100. Tange, Y.; Nishihara, Y.; Tsuchiya, T. Unified analyses for P–V–T equation of state of MgO: A solution for pressure-scale problems in high P–T experiments. *J. Geophys. Res. Solid Earth* **2009**, *114*, B03208. [[CrossRef](#)]
101. Otero-de-la-Roza, A.; Luaña, V. Treatment of first-principles data for predictive quasiharmonic thermodynamics of solids: The case of MgO. *Phys. Rev. B* **2011**, *84*, 024109. [[CrossRef](#)]
102. Srivastava, S.K. Analysis of thermoelastic constants of solids and minerals at high temperatures. *J. Phys. Chem. Solids* **2006**, *67*, 2275–2281. [[CrossRef](#)]
103. Stacey, F.D. A thermal model of the Earth. *Phys. Earth Planet. Inter.* **1977**, *15*, 341–348. [[CrossRef](#)]
104. Brown, J.M.; Shankland, T.J. Thermodynamic parameters in the Earth as determined from seismic profiles. *Geophys. J. Int.* **1981**, *66*, 579–596. [[CrossRef](#)]
105. Karki, B.B. Thermal pressure in MgO and MgSiO₃ perovskite at lower mantle conditions. *Am. Mineral.* **2000**, *85*, 1447–1451. [[CrossRef](#)]
106. Stacey, F.D.; Isaak, D.G. Anharmonicity in mineral physics: A physical interpretation. *J. Geophys. Res. Solid Earth* **2003**, *108*, 2440. [[CrossRef](#)]
107. Scanavino, I.; Prencipe, M. Ab-initio determination of high-pressure and high-temperature thermoelastic and thermodynamic properties of low-spin (Mg_{1-x}Fe_x)O ferropericlase with x in the range [0.06, 0.59]. *Am. Mineral.* **2013**, *98*, 1270–1278. [[CrossRef](#)]
108. Merli, M.; Sciascia, L.; Pavese, A.; Diella, V. Modelling of thermo-chemical properties over the sub-solidus MgO-FeO binary, as a function of iron spin configuration, composition and temperature. *Phys. Chem. Miner.* **2015**, *42*, 347–362. [[CrossRef](#)]
109. Merli, M.; Bonadiman, C.; Diella, V.; Pavese, A. Lower mantle hydrogen partitioning between periclase and perovskite: A quantum chemical modelling. *Geochim. Cosmochim. Acta* **2016**, *173*, 304–318. [[CrossRef](#)]
110. Merli, M.; Bonadiman, C.; Diella, V.; Sciascia, L.; Pavese, A. Fe-periclase reactivity at Earth’s lower mantle conditions: Ab-initio geochemical modelling. *Geochim. Cosmochim. Acta* **2017**, *214*, 14–29. [[CrossRef](#)]
111. Pavese, A.; Diella, V. Uncertainties on elastic parameters and occupancy factors: How do they affect the accuracy of the calculated Gibbs free energy of minerals at (P,T) conditions? The case of 3T- versus 2M₁-phengite. *Phys. Chem. Miner.* **2007**, *34*, 637–645. [[CrossRef](#)]
112. Ganguly, J. *Thermodynamics in Earth and Planetary Sciences*; Springer: Berlin/Heidelberg, Germany, 2008; pp. 145–147.
113. Helffrich, G.; Connolly, J.A.D. Physical contradictions and remedies using simple polythermal equations of state. *Am. Mineral.* **2009**, *94*, 1616–1619. [[CrossRef](#)]
114. Jacobs, M.H.G.; van den Berg, A.P.; de Jong, B.H.W.S. The derivation of thermo-physical properties and phase equilibria of silicate materials from lattice vibrations: Application to convection in the Earth’s mantle. *Calphad* **2006**, *30*, 131–146. [[CrossRef](#)]
115. Brosh, E.; Makov, G.; Shneck, R.Z. Application of CALPHAD to high pressures. *Calphad* **2007**, *31*, 173–185. [[CrossRef](#)]
116. Brosh, E.; Shneck, R.Z.; Makov, G. Explicit Gibbs free energy equation of state for solids. *J. Phys. Chem. Solids* **2008**, *69*, 1912–1922. [[CrossRef](#)]
117. Karbasi, A.; Saxena, S.K.; Hrubiak, R. The thermodynamics of several elements at high pressure. *Calphad* **2011**, *35*, 72–81. [[CrossRef](#)]
118. Holland, T.J.B.; Powell, R. An improved and extended internally consistent thermodynamic dataset for phases of petrological interest, involving a new equation of state for solids. *J. Metamorph. Geol.* **2011**, *29*, 333–383. [[CrossRef](#)]

119. Tirone, M. On the use of thermal equations of state and the extrapolation at high temperature and pressure for geophysical and petrological applications. *Geophys. J. Int.* **2015**, *202*, 55–66. [[CrossRef](#)]
120. Welche, P.R.L.; Heine, V.; Dove, M.T. Negative thermal expansion in beta-quartz. *Phys. Chem. Miner.* **1998**, *26*, 63–77. [[CrossRef](#)]
121. Bina, C.R.; Helffrich, G. Phase transition Clapeyron slopes and transition zone seismic discontinuity topography. *J. Geophys. Res. Solid Earth* **1994**, *99*, 15853–15860. [[CrossRef](#)]
122. Deuss, A.; Redfern, S.A.T.; Chambers, K.; Woodhouse, J.H. The nature of the 660-kilometer discontinuity in Earth's mantle from global seismic observations of PP precursors. *Science* **2006**, *311*, 198–201. [[CrossRef](#)] [[PubMed](#)]
123. Dziewonski, A.M.; Anderson, D.L. Preliminary Reference Earth Model. *Phys. Earth Planet. Inter.* **1981**, *25*, 297–356. [[CrossRef](#)]
124. Ito, E.; Takahashi, E. Postspinel transformations in the system Mg_2SiO_4 - Fe_2SiO_4 and some geophysical implications. *J. Geophys. Res. Solid Earth* **1989**, *94*, 10637–10646. [[CrossRef](#)]
125. Ito, E.; Akaogi, M.; Topor, L.; Navrotsky, A. Negative pressure-temperature slopes for reactions forming $MgSiO_3$ perovskite from calorimetry. *Science* **1990**, *249*, 1275–1278. [[CrossRef](#)] [[PubMed](#)]
126. Akaogi, M.; Ito, E. Refinement of enthalpy measurement of $MgSiO_3$ perovskite and negative pressure-temperature slopes for perovskite-forming reactions. *Geophys. Res. Lett.* **1993**, *20*, 1839–1842. [[CrossRef](#)]
127. Irifune, T.; Nishiyama, N.; Kuroda, K.; Inoue, T.; Isshiki, M.; Utsumi, W.; Funakoshi, K.; Urakawa, S.; Uchida, T.; Katsura, T.; et al. The postspinel phase boundary in Mg_2SiO_4 determined by in situ X-ray diffraction. *Science* **1998**, *279*, 1698–1700. [[CrossRef](#)] [[PubMed](#)]
128. Shim, S.-H.; Duffy, T.S.; Shen, G. The post-spinel transformation in Mg_2SiO_4 and its relations to the 660-km seismic discontinuity. *Nature* **2001**, *411*, 571–574. [[CrossRef](#)] [[PubMed](#)]
129. Katsura, T.; Yamada, H.; Shinmei, T.; Kubo, A.; Ono, S.; Kanzaki, M.; Yoneda, A.; Walter, M.J.; Ito, E.; Urakawa, S.; et al. Post-spinel transition in Mg_2SiO_4 determined by high P–T in situ X-ray diffractometry. *Phys. Earth Planet. Inter.* **2003**, *136*, 11–24. [[CrossRef](#)]
130. Fei, Y.; Van Orman, J.; Li, J.; van Westrenen, W.; Sanloup, C.; Minarik, W.; Hirose, K.; Komabayashi, T.; Walter, M.; Funakoshi, K. Experimentally determined postspinel transformation boundary in Mg_2SiO_4 using MgO as an internal pressure standard and its geophysical implications. *J. Geophys. Res. Solid Earth* **2004**, *109*, B02305. [[CrossRef](#)]
131. Akaogi, M.; Takayama, H.; Kojitani, H.; Kawaji, H.; Atake, T. Low-temperature heat capacities, entropies and enthalpies of Mg_2SiO_4 polymorphs, and α - β - γ and post-spinel phase relations at high pressure. *Phys. Chem. Miner.* **2007**, *34*, 169–183. [[CrossRef](#)]
132. Ishii, T.; Kojitani, H.; Akaogi, M. Post-spinel transitions in pyrolyte and Mg_2SiO_4 and akimotoite-perovskite transition in $MgSiO_3$: Precise comparison by high-pressure high-temperature experiments with multi-sample cell technique. *Earth Planet. Sci. Lett.* **2011**, *309*, 185–197. [[CrossRef](#)]
133. Ghosh, S.; Ohtani, E.; Litasov, K.D.; Suzuki, A.; Dobson, D.; Funakoshi, K. Effect of water in depleted mantle on post-spinel transition and implication for 660 km seismic discontinuity. *Earth Planet. Sci. Lett.* **2013**, *371*, 103–111. [[CrossRef](#)]
134. Kojitani, H.; Inoue, T.; Akaogi, M. Precise measurements of enthalpy of postspinel transition in Mg_2SiO_4 and application to the phase boundary calculation. *J. Geophys. Res. Solid Earth* **2016**, *121*, 729–742. [[CrossRef](#)]
135. Chopelas, A.; Boehler, R.; Ko, T. Thermodynamics and behavior of γ - Mg_2SiO_4 at high pressure: Implications for Mg_2SiO_4 phase equilibrium. *Phys. Rev. Lett.* **1997**, *78*, 4063–4066. [[CrossRef](#)]
136. Belousov, R. Ab-initio Quantum-Mechanical Simulation of Earth Minerals at Extreme Conditions of Temperature and Pressure. Ph.D. Thesis, University of Torino, Torino, Italy, 2011; p. 91, unpublished.
137. Yu, Y.; Wentzcovitch, R.M.; Tsuchiya, T.; Umemoto, K.; Weidner, D.J. First principles investigation of the postspinel transition in Mg_2SiO_4 . *Geophys. Res. Lett.* **2007**, *34*, L10306. [[CrossRef](#)]
138. Hernández, E.R.; Alfè, D.; Brodholt, J. The incorporation of water into lower-mantle perovskites: A first-principles study. *Earth Planet. Sci. Lett.* **2013**, *364*, 37–43. [[CrossRef](#)]
139. Hernández, E.R.; Brodholt, J.; Alfè, D. Structural, vibrational and thermodynamic properties of Mg_2SiO_4 and $MgSiO_3$ minerals from first-principles simulations. *Phys. Earth Planet. Inter.* **2015**, *240*, 1–24. [[CrossRef](#)]

140. Jacobs, M.H.G.; Schmid-Fetzer, R.; van den Berg, A.P. Phase diagrams, thermodynamic properties and sound velocities derived from a multiple Einstein method using vibrational densities of states: An application to MgO-SiO₂. *Phys. Chem. Miner.* **2017**, *44*, 43–62. [[CrossRef](#)]
141. Parisi, F.; Sciascia, L.; Princivalle, F.; Merli, M. The pressure-induced ringwoodite to Mg-perovskite and periclase post-spinel phase transition: A Bader's topological analysis of the ab initio electron densities. *Phys. Chem. Miner.* **2012**, *39*, 103–113. [[CrossRef](#)]
142. Shearer, P.M.; Flanagan, M.P. Seismic velocities and density jumps across the 410- and 660-kilometer discontinuities. *Science* **1999**, *285*, 1545–1548. [[CrossRef](#)] [[PubMed](#)]
143. Cammarano, F.; Romanowicz, B. Insights into the nature of the transition zone from physically constrained inversion of long-period seismic data. *Proc. Natl. Acad. Sci. USA* **2007**, *104*, 9139–9144. [[CrossRef](#)] [[PubMed](#)]
144. Agee, C.B. Petrology of the mantle transition zone. *Annu. Rev. Earth Planet. Sci.* **1993**, *21*, 19–41. [[CrossRef](#)]
145. Agee, C.B. Phase transformations and seismic structure in the upper mantle and transition zone. In *Ultrahigh-Pressure Mineralogy: Physics and Chemistry of the Earth's Deep Interior. Reviews in Mineralogy*; Hemley, R.J., Ed.; Mineralogical Society of America: Chantilly, VA, USA, 1998; Volume 37, pp. 165–203.
146. Vacher, P.; Mocquet, A.; Sotin, C. Computation of seismic profiles from mineral physics: The importance of non-olivine components for explaining the 660 km depth discontinuity. *Phys. Earth Planet. Inter.* **1998**, *106*, 275–298. [[CrossRef](#)]
147. Weidner, D.J.; Wang, Y. Chemical- and Clapeyron-induced buoyancy at the 660 km discontinuity. *J. Geophys. Res. Solid Earth* **1998**, *103*, 7431–7441. [[CrossRef](#)]
148. Hirose, K. Phase transitions in pyrolitic mantle around 670-km depth: Implications for upwelling of plumes from the lower mantle. *J. Geophys. Res. Solid Earth* **2002**, *107*, 2078. [[CrossRef](#)]
149. Dobson, D.P.; Jacobsen, S.D. The flux growth of magnesium silicate perovskite single crystals. *Am. Mineral.* **2004**, *89*, 807–811. [[CrossRef](#)]
150. Sasaki, S.; Prewitt, C.T.; Sato, Y.; Ito, E. Single-crystal X-ray study of γ -Mg₂SiO₄. *J. Geophys. Res. Solid Earth* **1982**, *87*, 7829–7832. [[CrossRef](#)]



© 2017 by the author. Licensee MDPI, Basel, Switzerland. This article is an open access article distributed under the terms and conditions of the Creative Commons Attribution (CC BY) license (<http://creativecommons.org/licenses/by/4.0/>).